J. Fluid Mech. (2024), *vol*. 1001, A45, doi:10.1017/jfm.2024.786

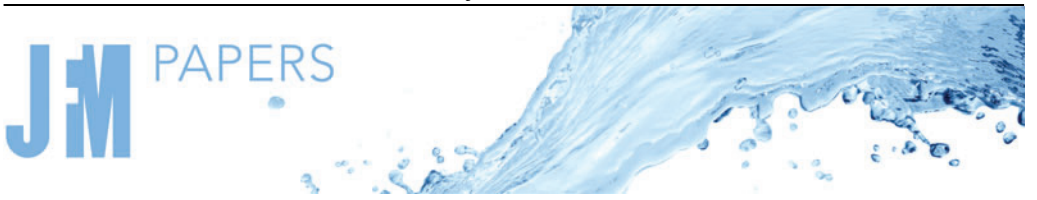

Dust-free region over horizontal hot surfaces

K.K. Prasoon[1],†, **Anubhab Roy**[1] **and Baburaj A. Puthenveettil**[1]

[1]Department of Applied Mechanics, Indian Institute of Technology Madras, Chennai 600036, India

(Received 7 April 2023; revised 24 June 2024; accepted 26 June 2024)

We study the formation of dust-free regions above hot horizontal surfaces of uniform temperature and propose relations for its height in the limit of small particle inertia and gravitational effects. By including particle inertia, thermophoretic, gravitational and viscous effects, we conduct Lagrangian simulations of particle dynamics in a natural convection boundary layer over a horizontal surface. Trajectory analysis of the particles inside the boundary layer on the surface reveals the existence of two separatrices originating from a saddle point, which form the boundary of the dust-free region. These separatrices for low gravitational effects follow the boundary layer thickness, but are of much lower height and also depend on the dimensionless thermophoretic number (Th) and Prandtl number (Pr). We obtain a relation for the dimensionless height of the dust-free region (η_{df}) as a function of Pr and Th, for low dimensionless gravitational number (Gn); the numerical solution of this equation gives us the dust-free region height for any Th and Pr. We then obtain scaling laws for η_{df} using the boundary layer equations corresponding to the $Pr \gg 1$ and $Pr \ll 1$ cases; these scaling laws are shown to be valid respectively for $Pr > 1$ and $Pr < 1$, except in the large η limit for $Pr > 1$, where η is the boundary layer similarity variable. We then obtain an empirical relation in this large η limit using the numerical solutions of the boundary layer equations for the intermediate Pr case to obtain scaling laws for dust-free region height for the whole range of $Pr \ll 1$ to $Pr \gg 1$.

Key words: Bénard convection, particle/fluid flow, buoyant boundary layers

1. Introduction

In Rayleigh–Bénard convection (RBC) of smoke laden air (Puthenveettil *et al.* 2011; Gunasegarane & Puthenveettil 2014), as shown in figure 1(*a*), dark plumes are seen when a horizontal laser sheet is passed through a plane parallel and close to the bottom hot plate. A side view of one such dark line in the top view, observed with a vertical laser

† Email address for correspondence: kkprasoon90@gmail.com

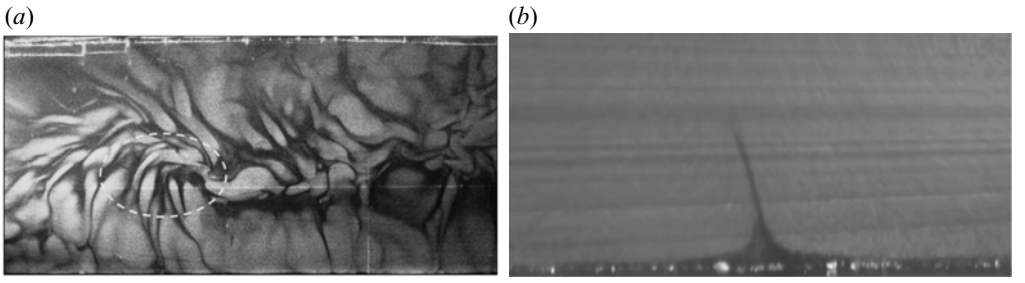

Figure 1. Images of dust-free regions over horizontal hot surfaces in natural convection: (*a*) top view of dust-free plumes seen as dark lines in visualisations with a horizontal laser sheet close to the hot plate (Gunasegarane & Puthenveettil 2014); (*b*) an image that was captured for the present work, showing the side view of two dust-free regions inside the boundary layer turning into a plume.

sheet (see figure 1*b*), shows boundary layer like, particle-free regions that appear dark, which later turn upwards to give rise to the dark plumes in the top view. The presence of such 'dust-free' regions, even though helpful in visualisations, prevents tracer-based measurements of the near-wall phenomena in turbulent convection; a critical requirement for clarifying the phenomenology of turbulent convection. In addition to the fundamental importance of understanding these phenomena, formation and scaling of such dust-free regions near horizontal hot surfaces is important in several industrial applications, like electronic manufacturing (Stratmann *et al.* 1988; Besling, Van der Put & Schoonman 1995), heat transfer by nanofluids (Putra, Roetzel & Das 2003), soot removal in combustion (Eisner & Rosner 1985), aerosol deposition in nuclear reactors (Fernandes & Loyalka 1996), dust samplers (Wen & Wexler 2007) and preventing dust deposition on solar photovoltaic cells (Gupta *et al.* 2019; Oh, Figgis & Rashkeev 2020). Many natural phenomena of importance like settling and re-suspension of atmospheric dust particles (Nicholson 1988), as well as crystal settling in magma chambers (Martin & Nokes 1988), also depend on an understanding of this phenomenon which occurs near hot surfaces. In this paper, using Lagrangian simulations of a particle-laden natural convection boundary layer on a horizontal hot surface, we show that the particle migration from the hot surface due to the temperature gradient could be one of the possible reasons for the occurrence of such 'dust-free' regions near horizontal hot surfaces. We then obtain the scaling for the extent of such dust-free regions above horizontal hot surfaces as a function of the relevant dimensionless numbers.

Migration of small particles away from hot surfaces, known as thermophoresis, is a phenomenon known for over a century (Tyndall 1870; Aitken 1884); see Talbot *et al.* (1980) for a review. Such a migration, due to the collision between higher kinetic energy gas molecules from the hotter side of the fluid and the particle surfaces, which could give rise to dust-free regions near hot surfaces, has also been known for a long time (Cawood 1936). Extensive studies on particle interaction with shear dominant, forced convection boundary layers have been conducted, often with the intention of obtaining the particle deposition rate for cold surfaces (Homsy, Geyling & Walker 1981; Batchelor & Shen 1985; Gokoglu & Rosner 1986). The extent of the dust-free region over the hot surfaces in such flows were obtained by Goren (1977) by numerically solving the particle concentration equations along with the similarity equations of forced convection boundary layers. They found that for a given thermophoretic coefficient, wall temperature T_w and Prandtl number Pr, the bounding curve of the dust-free space scaled in the same way as the boundary layer thickness; the dependence of the dust-free region on these three parameters was

however left undetermined. Measurements of the dust-free region in forced convection by Talbot *et al.* (1980) also showed that the dust-free region thickness δ_{df} is parallel to the boundary layer thickness δ, but smaller. Hereinafter, the subscript df indicates the dust-free region. However, in contrast to the observations of Goren (1977), they found δ_{df} to be independent of T_w and the free stream velocity U_∞. Recently, Oh *et al.* (2020), in a similar analysis as that of Talbot *et al.* (1980) but including gravitational effects, showed that the particle trajectory deviates from the fluid trajectory and can form dust-free regions over hot surfaces in forced convection, when the temperature differences are sufficient. Clearly, no conclusive scaling of the dust-free region height is yet available even in shear dominant, forced convection boundary layers.

When buoyancy becomes dominant in these boundary layers, the dynamics become more involved since the temperature difference drives the flow as well as the thermophoresis; such studies have been limited. Most studies on such natural convection boundary layers limit their analysis to vertical surfaces alone (Zernik 1957; Epstein, Hauser & Henry 1985; Nazaroff & Cass 1987), where the thermophoretic and the gravitational forces are perpendicular to each other, and the gravitational settling does not directly affect the dust-free region. For such natural convection boundary layers over vertical surfaces, using the fluid flow field given by an earlier similarity solution, by balancing the thermophoretic force with the Stokes drag, Zernik (1957) proposed that the dimensionless dust-free region scaled as $\eta_{df} = f(T')$, where η_{df} is the value of η, the similarity variable for the flow, at the dust-free region edge and $f(T')$ is a function of the dimensionless temperature difference $T' = 2T_w/\Delta T_w$, with $\Delta T_w = T_w - T_\infty$, where T_∞ is the ambient temperature. Zernik's (1957) result, however, does not quantify the effects of the ratio of the fluid and the particle thermal conductivities k_f/k_p and the Knudsen number $Kn = \lambda/a$, where λ is the mean free path of the gas and a is the particle radius; k_f/k_p and Kn do affect η_{df} through their influence on the thermophoretic force. Additionally, Zernik's (1957) result also does not include the effects of Prandtl number $Pr = \nu/\alpha$, the ratio of kinematic viscosity of the fluid to its thermal diffusivity.

When such buoyancy dominant boundary layers occur on horizontal surfaces, as in RBC and the other applications mentioned above, the presence or absence of such particle-free regions and the scaling of such regions depend on complex interactions among the gravitational settling, the thermophoretic force exerted by the temperature gradient in the boundary layer, the inertia and the viscous drag exerted by the boundary layer, and for larger and denser particles, on the inertia of the particles. Studies on the interaction of such natural convection boundary layers on horizontal surfaces with particles are rare, in spite of their common occurrence and importance in many industrial applications. In the only available study, assuming similarity, Guha & Samanta (2014) solved the boundary layer particle concentration equation along with the natural convection boundary layer equations for a horizontal plate in an Eulerian framework, and showed that when Brownian effects are negligible, in the absence of gravitational settling, at a specific temperature difference, a particle-free region is formed close to the hot surface at a constant value of the similarity variable η. However, the study neglected particle inertia, which has been shown to create deviations in particle trajectories from the flow streamlines (Maxey & Corrsin 1986). Further, the assumption of thermophoretic diffusion coefficients and the unrealistic particle concentration boundary condition at the wall, makes their simulations approximate; Guha & Samanta (2014) also did not provide a scaling for the particle-free region.

It is hence clear that scaling of the extent of particle-free regions near horizontal surfaces, where buoyancy is predominant so that natural convection boundary layers form,

is poorly understood; such a situation occurs in many applications of importance. In the present work, we study the interaction of spherical point particles with a two-dimensional natural convection boundary layer that forms on a horizontal hot surface. We use a Lagrangian approach of solving the Maxey & Riley (1983) equation for small volume fraction of particles, when Brownian motion is negligible, for the flow field given by the similarity solutions of Rotem & Claassen (1969). Since the similarity solutions of Rotem & Claassen (1969) approximate the flow in the local boundary layers on either side of the line plumes on the hot plate in RBC at intermediate Rayleigh numbers (Ra) (Theerthan & Arakeri 1998; Puthenveettil & Arakeri 2005), the present study is expected to model the formation of dust-free regions in the natural convection boundary layer over a hot horizontal plate and in the local boundary layers on the hot plate in RBC, both at intermediate Ra. By including inertia of the particles and the gravitational forces on them, we obtain realistic particle trajectories from these simulations. The particle trajectories show the formation of particle-free regions close to the hot surface for finite values of the thermophoretic number,

$$Th = \frac{C_T C_B \Delta T_w \sqrt{Pr}}{\langle T \rangle}, \tag{1.1}$$

where C_B is a particle slip correction factor and C_T is the thermophoretic coefficient in (2.2), which is a function of k_f/k_p and Kn, as given by Talbot *et al.* (1980). We show that the longitudinal extent of the dust-free region reduces with increasing ratio of gravitational settling velocity (u_g) to the characteristic boundary layer velocity (U_w); we define this ratio as the gravitational number Gn in (2.13) and (2.15). With increase in Gn, at any given Th, particles settle beyond decreasing distances. For small values of Gn, when gravitational settling is negligible, by obtaining an expression for a separatrix, which we observe to occur always at the dust-free region boundary, we obtain a scaling for the dust-free region height. The obtained scaling of the dust-free region height shows that the dust-free region boundary is parallel to the boundary layer edge, but smaller in height. The ratio of the dust-free region height to the boundary layer height is shown to be a function of Th and Pr; we obtain these functions for small, intermediate and large Pr.

The paper is organised as follows. We formulate the dimensionless particle motion equation in § 2.1, where the relevant dimensionless numbers that determine the particle motion are obtained; the limiting case of the equation for small Stokes number ($\widehat{St}$) is discussed in § 2.2. The natural convection boundary layer flow and the temperature fields given by Rotem & Claassen (1969) are briefly discussed in § 2.3, with the numerical method of solution of the particle motion equation discussed in § 2.4. Section 3.1 discusses the particle trajectories and the variation of the extents of the dust-free regions for various finite Th and Gn, along with the formation of the separatrix at the boundary of the dust-free region. An expression for the separatrix, as well as the scaling for the dust-free region height in the small and the large η limits, are obtained for $Gn \ll Th$ and $\widehat{St} \ll 1$ in § 3.3. In § 4, explicit scaling laws for small Pr, large Pr and intermediate values of Pr are proposed for the dust-free region height when $Gn = 0$, before concluding in § 5.

2. Formulation

2.1. *Particle motion equation*

We formulate the governing equation for the particle motion in natural convection over hot surfaces by adding thermophoretic force to the Maxey & Riley (1983) equation; the corresponding formulation for forced convection was done by Talbot *et al.* (1980).

For high density, micron sized aerosol particles, as the Basset–Boussinesq history force is much smaller compared with the viscous drag term in the dimensionless Maxey & Riley (1983) equation, we neglect this history force (Bergougnoux *et al.* 2014). Since the particle sizes that we consider are small, Faxen's correction, $(-a^2/6)\nabla^2 u$, to the viscous drag can also be neglected (Maxey & Riley 1983) in comparison to the terms that are linear in fluid and particle velocities. The governing equation then reduces to

$$\rho_p \frac{\mathrm{d}\boldsymbol{v}}{\mathrm{d}t} = \rho_f \frac{\mathrm{D}\boldsymbol{u}}{\mathrm{D}t} - \frac{9}{2}\frac{\mu}{a^2}\frac{1}{C_B}(\boldsymbol{v}-\boldsymbol{u}) - \frac{\rho_f}{2}\left(\frac{\mathrm{d}\boldsymbol{v}}{\mathrm{d}t} - \frac{\mathrm{D}\boldsymbol{u}}{\mathrm{D}t}\right) - \frac{9\rho_f \nu^2}{a^2} C_T \frac{\boldsymbol{\nabla} T}{\langle T_p \rangle} + (\rho_p - \rho_f)\boldsymbol{g}, \tag{2.1}$$

where the term on the left-hand side is the particle inertia with $\mathrm{d}/\mathrm{d}t = \partial/\partial t + \boldsymbol{v}\cdot\boldsymbol{\nabla}$ being the material derivative along the particle trajectory and $\boldsymbol{v}$ the particle velocity vector. In the first term on the right in (2.1), $\mathrm{D}/\mathrm{D}t = \partial/\partial t + \boldsymbol{u}\cdot\boldsymbol{\nabla}$ is the material derivative along the fluid trajectory, with $\boldsymbol{u}$ being the fluid velocity vector. The second term on the right-hand side of (2.1) is the viscous drag where C_B is any appropriate slip correction factor, such as Basset or Cunningham slip correction factors, to accommodate non-continuum effects, and μ is the dynamic viscosity of the fluid. The third term on the right-hand side of (2.1) is the added mass, where ρ_f is the fluid density. The next term on the right is the thermophoretic force term, where T is the fluid temperature field and $\langle T_p \rangle$ the undisturbed fluid temperature at the particle centre if the particle was not present at that point. The thermophoretic coefficient in this term is

$$C_T = \frac{C_s(k_f/k_p + C_t Kn)}{(1+3C_m Kn)(1+2k_f/k_p + 2C_t Kn)}, \tag{2.2}$$

with the coefficients $C_m = 1.14$, $C_s = 1.17$ and $C_t = 2.18$ (Talbot *et al.* 1980); k_f and k_p being the fluid and particle thermal conductivities. An alternative expression for C_T in terms of Kn and k_f/k_p, given by Beresnev & Chernyak (1995), which was shown to be more accurate in the transition regime of Knudsen numbers by Guha & Samanta (2014), could also be used instead of (2.2). The last term in (2.1) is the buoyancy acting on the particle, where $\boldsymbol{g}$ is the acceleration vector due to gravity and ρ_p the particle density.

We normalise (2.1) with the characteristic scales near the hot plate in RBC (Theerthan & Arakeri 1998; Puthenveettil & Arakeri 2005), namely, the near-wall length scale

$$Z_w = \left(\frac{\nu\alpha}{g\beta\Delta T_w}\right)^{1/3}, \tag{2.3}$$

where β is the thermal expansivity of the fluid, the near-wall velocity scale

$$U_w = \frac{\sqrt{\nu\alpha}}{Z_w} \tag{2.4}$$

and the near-wall time scale

$$t_w = Z_w/U_w. \tag{2.5}$$

The dimensionless governing equation for particle motion then becomes

$$\frac{\mathrm{d}\boldsymbol{v}^*}{\mathrm{d}t^*} = \frac{3\epsilon}{2+\epsilon}\frac{\mathrm{D}\boldsymbol{u}^*}{\mathrm{D}t^*} - \frac{1}{\widehat{St}}(\boldsymbol{v}^* - \boldsymbol{u}^*) - \frac{1}{\widehat{St}} Th \boldsymbol{\nabla}^*\theta - \frac{1}{\widehat{St}} Gn\hat{\boldsymbol{j}}, \tag{2.6}$$

where all the starred variables denote the dimensionless variables corresponding to the dimensional variables in (2.1), $\epsilon = \rho_f/\rho_p$ and the dimensionless temperature,

$$\theta = \frac{T - T_\infty}{\Delta T_w}. \tag{2.7}$$

Equation (2.6) shows that the following dimensionless numbers determine the particle dynamics. The modified Stokes number, $\widehat{St}$ in (2.6) is

$$\widehat{St} = \frac{C_B(2+\epsilon)St}{2}, \tag{2.8}$$

where the Stokes number

$$St = \frac{2}{9}\frac{\rho_p a^2/\mu}{t_w} = \frac{2}{9}\frac{1}{\epsilon\sqrt{Pr}}Ra_p^{2/3}, \tag{2.9}$$

by using (2.5), (2.3) and (2.4). Here, the particle Rayleigh number,

$$Ra_p = \left(\frac{g\beta\Delta T_w a^3}{\nu\alpha}\right)^{1/3}, \tag{2.10}$$

is the ratio of the time scales of thermal transport by diffusion ($a^2/\sqrt{\nu\alpha}$) to the thermal transport by convection ($\sqrt{\nu\alpha}/g\beta\Delta T_w a$), both evaluated at the particle length scale. The thermophoretic number,

$$Th = \frac{1}{Re}\frac{C_T C_B \Delta T_w}{\langle T\rangle}, \tag{2.11}$$

in (2.6) represents the dimensionless strength of the thermophoretic effects on the particle, where the Reynolds number

$$Re = \frac{1}{2}\frac{U_w Z_w}{\nu} = \frac{1}{2\sqrt{Pr}}, \tag{2.12}$$

by using (2.3) and (2.4). In (2.6),

$$Gn = \frac{C_B(1-\epsilon)St}{Fr^2} = \frac{2(1-\epsilon)\widehat{St}}{(2+\epsilon)Fr^2} \tag{2.13}$$

is the gravitational number, where the Froude number

$$Fr = \frac{U_w}{\sqrt{gZ_w}}. \tag{2.14}$$

By using (2.8), (2.9) and (2.14) in (2.13),

$$Gn = \frac{C_B\frac{4}{3}\pi a^3(\rho_p - \rho_f)g}{6\pi\mu a}\frac{1}{U_w} = \frac{u_g}{U_w} = u_g^*, \tag{2.15}$$

where u_g^* is the dimensionless gravitational settling velocity and u_g the gravitational settling velocity. Typical values of these dimensionless numbers for olive oil droplets in air are tabulated in table 1 for different diameters of droplets. We note that $\widehat{St} \ll 1$ for the common droplet sizes in aerosols. We have ignored the role of particle interactions and

Droplet Dia (μm)	$\widehat{St}$	Th	Gn	Ra_p
0.1	2×10^{-9}	2×10^{-2}	1×10^{-7}	1×10^{-13}
1	7×10^{-8}	4×10^{-3}	4×10^{-6}	1×10^{-10}
5	2×10^{-6}	1×10^{-3}	1×10^{-4}	1.25×10^{-8}

Table 1. Values of the various dimensionless numbers for olive oil droplets in air at $Pr = 0.7$ for $\Delta T_w \approx 10$ K and $\langle T \rangle \approx 300$ K.

inertial lift forces in the present formulation, effects that could lead to the modification of particle trajectories. Both hydrodynamic and non-hydrodynamic interactions between aerosol particles can play a significant role in the trajectories of aerosol particles, which subsequently influences phenomena like coagulation and deposition (see Patra, Koch & Roy 2022 and references therein). In the present study, we are interested in the highly dilute limit; thus, the role of interactions is neglected. A particle has a non-zero slip with respect to the local fluid velocity; for small St, the deviation is due to the thermophoretic velocity (to be discussed in detail in the next section). Since a particle has a non-zero slip velocity in a local shear flow, it could experience an inertial lift force as was derived in the case of a simple shear flow by Saffman (1965) (see Candelier, Mehlig & Magnaudet 2019 for more extensions to more general linear flows). The relative magnitude of the Saffman lift force would depend on the particle Reynolds number defined based on the local shear rate, Re_γ. In the present problem, $Re_\gamma = Ra_p^2/\sqrt{Pr}$. From the listed values of Ra_p in table 1, we see $Re_\gamma \ll 1$ and thus, the effect of inertial lift is negligible in the present study. This assumption is further corroborated by Yang *et al.* (2022) where they found the effect of Saffman lift negligible in the study of particle dynamics in Rayleigh–Bénard convection.

2.2. *Limiting cases*

When $\widehat{St} \ll 1$, the first term on the right-hand side of (2.6) can be neglected since $1/\widehat{St}$ appears on all the other terms on the right-hand side of (2.6). Then, since $\boldsymbol{v}^* = \mathrm{d}\boldsymbol{x}^*/\mathrm{d}t^*$, for $\widehat{St} \ll 1$, (2.6) reduces to

$$\widehat{St}\frac{\mathrm{d}^2\boldsymbol{x}^*}{\mathrm{d}t^{*2}} = -\left(\frac{\mathrm{d}\boldsymbol{x}^*}{\mathrm{d}t^*} - \boldsymbol{u}^*\right) - Th\nabla^*\theta - \widehat{St}\frac{Gn}{\widehat{St}}\hat{j}. \tag{2.16}$$

In (2.16), $\widehat{St}$ can approach zero only if St is approaching zero, as shown by (2.8). Hence, when $\widehat{St} \to 0$, since both $\widehat{St}$ and Gn have a similar dependence on St, as evident from (2.8) and (2.13), $Gn/\widehat{St}$ can still remain finite depending on the values that ϵ and Fr^2 take. So when $\widehat{St} \to 0$ (or $St = 0$), the first and the last terms in (2.16) are negligible whereas the second and the third terms remain finite. Further, the term $-Th\nabla^*\theta$ in (2.16) can be re-written by using (2.12), (2.11) and (2.7) as

$$-Th\nabla^*\theta = -\frac{C_T C_B \Delta T_w}{Re\langle T\rangle}\nabla^*\theta = \frac{-2\nu C_T C_B \nabla T}{\langle T\rangle}\frac{1}{U_w} = \frac{\boldsymbol{u}_t}{U_w} = \boldsymbol{u}_t^*, \tag{2.17}$$

where $\boldsymbol{u}_t$ is the thermophoretic velocity and $\boldsymbol{u}_t^*$ its dimensionless form. Hence, when $\widehat{St} \to 0$, (2.16) reduces to

$$\boldsymbol{v}^* = \boldsymbol{u}^* - Th\nabla^*\theta = \boldsymbol{u}^* + \boldsymbol{u}_t^*, \tag{2.18}$$

the zeroth-order equation for the particle velocity. Equation (2.18) implies that when $\widehat{St} \to 0$, the particle velocity in fluid flows with finite temperature gradients, like thermal boundary layers and plumes, is a vector sum of the fluid velocity and the thermophoretic velocity. Note that this result holds even when $\epsilon \to 1$ for neutrally buoyant particles, usually employed in particle image velocimetry (PIV) studies. Therefore, even when $St = 0$, neutrally buoyant particles with $\epsilon = 1$ do not follow the fluid trajectory in regions where $\boldsymbol{u}_t^*$ is significant. Hence, PIV measurements inside regions like thermal boundary layers and plumes may not be reliable if $\boldsymbol{u}_t^*$ values there are not negligible. It is obvious from (2.16) that particles follow the fluid trajectory when $Gn \ll 1$, $Th \ll 1$ and $\widehat{St} = 0$, since $\boldsymbol{v}^* = \boldsymbol{u}^*$ in such a case. In all other cases, the particles would deviate from fluid trajectories under the influence of thermophoretic and gravitational forces, even when $St = 0$.

Since the fluid velocity field and the temperature field that we consider are steady, it can be noted from (2.18) that the particle velocity field also approaches a steady state as $\widehat{St} \to 0$. This is because in such a case, when $\widehat{St} \to 0$, the response time required for the particles to reach the velocity of the flow field becomes infinitely small due to the low inertia and hence, the time evolution of the particles in the unsteady state can be neglected in such a case. Then, the initial injection velocities of particles into the flow field become irrelevant in such cases.

2.3. *Fluid flow field*

We assume that the particles do not modify the flow around them, which is valid for the case of a dilute mixture of small particles, when mass loading of the particle phase is low (Guha 2008). It is shown in Appendix A that those conditions are valid in the present study. This assumption allows us to substitute an existing solution of natural convection boundary layers for $\boldsymbol{u}^*(x, y)$ and $\theta(x, y)$ in (2.16) to study the evolution of particles in that flow field. The natural convection boundary layer flow above a horizontal surface has been obtained by Rotem & Claassen (1969), Pera & Gebhart (1973) and Samanta & Guha (2012); we here use the similarity solutions proposed by Rotem & Claassen (1969).

Rotem & Claassen (1969) gave the dimensionless stream function,

$$\psi^*(\eta) = {x_{rc}^*}^{3/5} F(\eta), \tag{2.19}$$

and the dimensionless temperature difference,

$$H(\eta) = \theta = \frac{T - T_\infty}{\Delta T_w}, \tag{2.20}$$

as functions of the similarity variable

$$\eta = \hat{y} {x_{rc}^*}^{-2/5}. \tag{2.21}$$

Here, the dimensionless x coordinate,

$$x_{rc}^* = x/L, \tag{2.22}$$

where L is the length of the plate. The stretched y coordinate,

$$\hat{y} = y_{rc}^* Gr_L^{1/5} = \frac{y}{L} Gr_L^{1/5}, \tag{2.23}$$

where the Grashoff number

$$Gr_L = \frac{g\beta \Delta T_w L^3}{\nu^2} = \frac{Ra_L}{Pr}, \tag{2.24}$$

where $Ra_L = (-g\beta\Delta TL^3)/\nu\alpha$ is the Rayleigh number based on L, so that, using (2.21), (2.22), (2.23) and (2.24),

$$\eta = \frac{y}{L}\left(\frac{x}{L}\right)^{-2/5}\left(\frac{Ra_L}{Pr}\right)^{1/5} = \frac{y}{(x^2Z_w^3)^{1/5}}\frac{1}{Pr}. \tag{2.25}$$

From Rotem & Claassen's (1969) stretched horizontal and vertical velocity components, given in (D3) and (D4), we obtain the dimensionless velocity components for the present study as

$$u_x^* = \frac{\partial\psi^*}{\partial\hat{y}} = Pr^{1/10}x^{*1/5}F'(\eta) \tag{2.26}$$

and

$$u_y^* = -\frac{\partial\psi^*}{\partial x_{rc}{}^*} = \frac{1}{5}Pr^{3/10}x^{*-2/5}(2\eta F'(\eta) - 3F(\eta)), \tag{2.27}$$

by using (D1), (B1), (B2), (2.3) and (2.4).

Values of $F(\eta)$ from (2.19) and $H(\eta)$ from (2.20) for various Pr are given by Rotem & Claassen (1969) by numerical solution of the natural convection boundary layer equations (2.28). The values of η, and hence the values of the velocity components (2.26), (2.27) and the temperatures (2.20) at any location inside the boundary layer are then determined by the values of Ra_L and Pr through (2.25). Here, $F(\eta)$ and $H(\eta)$ are obtained by numerically solving the following boundary layer equations of Rotem & Claassen (1969),

$$5F''' + 3FF'' - F'^2 = 2G - 2\eta G', \tag{2.28a}$$

$$H = G' \tag{2.28b}$$

and

$$H'' + \tfrac{3}{5}PrFH' = 0, \tag{2.28c}$$

where $'$ indicates derivative with respect to η. Additionally,

$$G(\eta) = \left(\frac{p - p_\infty}{\rho_\infty\nu^2}L^2 + \frac{gy_{rc}^*L^3}{\nu^2}\right)Gr^{-4/5}x_{rc}^{*\,-2/5} \tag{2.29}$$

is the dimensionless pressure function, where p is the local fluid pressure, p_∞ the pressure of the ambient fluid far away from the plate and ρ_∞ the corresponding density. The boundary conditions for solving (2.28) include

$$F = F' = 0, \quad H = G' = 1 \quad \text{at } \eta = 0 \tag{2.30a}$$

and

$$F' = H = G = 0 \quad \text{when } \eta \to \infty. \tag{2.30b}$$

2.4. *Numerical method*

Numerical solutions of (2.16) were obtained for 5000 particles, initially placed randomly in the domain with zero initial velocity at $\widehat{St} = 10^{-5}$ for different combinations of Gn and Th. The horizontal domain started at $x = 0.01Z_w$ (or $x^* = 0.01$) to exclude the origin of the boundary layer, which is a singular point. The domain extended horizontally up to $50Z_w$, approximately the average length of a growing boundary layer before it turns into a plume

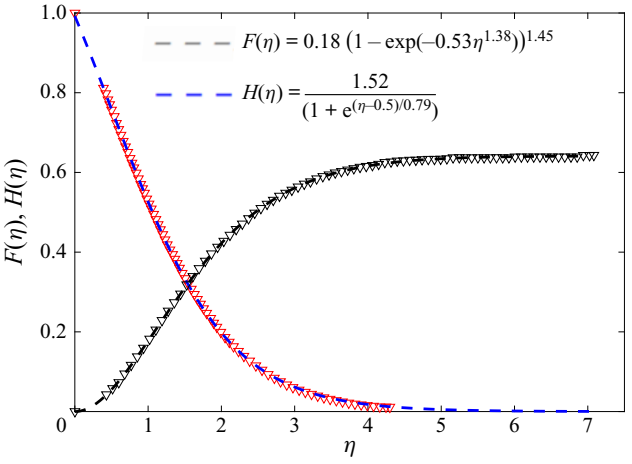

Figure 2. Comparison of the curve fits obtained for $F(\eta)$ and $H(\eta)$ to the data points obtained from Rotem & Claassen (1969) for $Pr = 0.7$. Data points from Rotem & Claassen (1969) for: $\triangledown$, $F(\eta)$; and red $\triangledown$, $H(\eta)$. Curve fits for: black – – –, $F(\eta)$; and blue – – –, $H(\eta)$.

(Theerthan & Arakeri 1998). In the vertical direction, since the boundary layer thickness $\delta \sim Z_w$, the domain extended from $y = 0$ to $y = 40Z_w$ to ensure that both the thermal and the velocity boundary layers were well within the domain.

To maintain a constant number of particles in the domain, whenever a particle exited, another particle was introduced through the top of the domain at a random x position with zero velocity. As discussed in § 2.2, the initial velocities of the particles become insignificant when $\widehat{St} \ll 1$, as they reach the surrounding fluid velocity in a negligible amount of time. Therefore, the initial velocities at the start of the computation and the injection velocities of particles through the top boundary were set to zero for convenience.

Equation (2.16) was numerically solved using the fifth-order Runge–Kutta method with adaptive step size selection, implemented via the ODE45 tool in MATLAB®. The particles evolved in the steady flow field described by (2.26), (2.27) and (2.20). To solve (2.16) for particle positions, u_x^* in (2.26), u_y^* in (2.27) and θ in (2.20) were obtained by interpolating the solutions of the boundary layer equations (2.28). For efficient implementation of interpolation, (2.16) was integrated using a curve-fitted form of $F(\eta)$ and $H(\eta)$, which were used to obtain u_x^* in (2.26), u_y^* in (2.27) and θ in (2.20). The fits for $F(\eta)$ and $H(\eta)$ are shown in figure 2.

The ODE45 algorithm automatically selects smaller time steps where the solutions change abruptly, ensuring the accuracy of the solution based on the specified tolerance. The current simulations were conducted with a relative tolerance of 10^{-6}. Solving the trajectory of a particle from one end of the domain to the other took approximately 5 minutes. Since each particle trajectory could be independently solved using multiple threads in parallel, the computational time was drastically reduced.

The curve fits in figure 2 for $Pr = 0.7$ were used only to obtain the particle dynamics discussed in § 3. The scaling laws in the subsequent sections were derived using $F(\eta)$ and $H(\eta)$ obtained from numerical solutions of the boundary layer equations in (2.28).

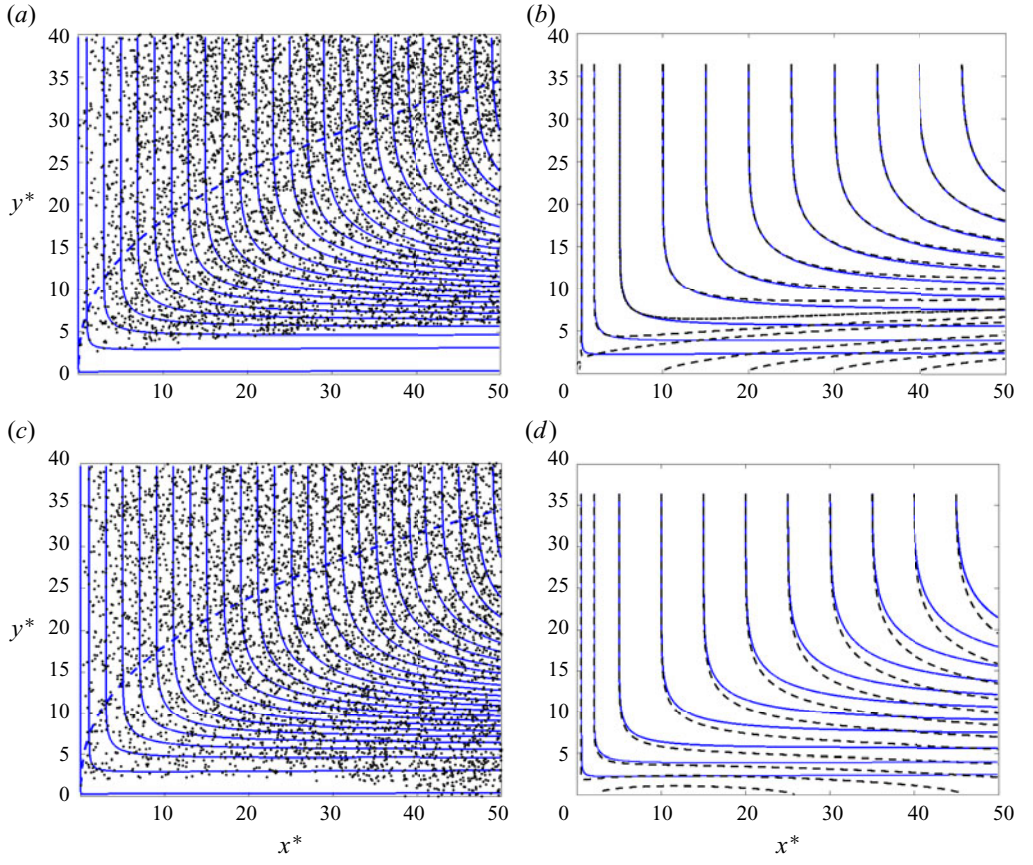

Figure 3. For $Gn = 0$ and $Th = 1$: (*a*) instantaneous particle positions and fluid streamlines; (*b*) fluid streamlines and particle trajectories. (*c*,*d*) The same for $Gn = 0.14$ and $Th = 1$; blue ——, fluid stream lines; blue – – – –, velocity boundary layer edge; – – – –, particle trajectories; Please refer to the particle motion videos corresponding to panel (*a*) at $Gn = 0$ and to panel (*c*) at $Gn = 0.14$, provided in the supplementary movies, to see the evolution of particle positions.

3. Particle dynamics

3.1. *Flow streamlines and particle trajectories*

We analysed the dynamics of particles inside the boundary layer at $\widehat{St} = 10^{-5}$ for different combinations of Gn and Th. Figure 3(*a*) shows the particle positions and fluid's streamlines, while figure 3(*b*) shows the particle trajectories and fluid streamlines corresponding to $Gn = 0$ and $Th = 1$ at $t^* = 45$. Figure 3(*c*,*d*) shows the same at $Gn = 0.14$ and $Th = 1$ at $t^* = 60$. The corresponding motion of particles can be clearly viewed in the supplementary movies for the cases with and without gravity. The particle trajectories in figure 3(*b*,*d*) and the motion of the particles in the two videos corresponding to them show that the particles at the top of the domain are initially dragged down by the entrainment fluid flow into the boundary layer. For the low-gravitational-force situations, as in figure 3(*a*), once the particles enter the boundary layer, they mostly take a right turn before finally exiting the domain through the right end. For cases when Gn is non-negligible compared with Th, as in figure 3(*c*), many of the particles settle on the plate, as they move to the right; the location of settling depends on the relative strength of the gravitational force that the particles experience.

In figure 3(*a*,*c*), we see a dust-free region within the boundary layer, which forms under the influence of thermophoretic force. Both the figures show the final steady-state situation, after the initial transient development of the dust-free region is completed, which takes a dimensionless time of approximately $t^* \sim 50$. In figure 3(*a*), for the $Gn = 0$ case, we see a dust-free region that keeps growing in height as we move along the positive x direction; there is no settling of particles on the hot surface. For this case, the height of the dust-free region at any given x depends on the particular value of Th. In contrast, the height of the dust-free region in figure 3(*c*), after an initial increase, keeps decreasing as x increases. In the finite Gn case, the dust-free region ends at a finite distance from the origin of the boundary layer, beyond which the particles start to settle under the influence of gravity; the length of this dust-free region in figure 3(*c*) is approximately $x^* = 45$. We observed that if Gn is increased, the particles start to settle at a shorter x^* making the dust-free region smaller in size and height; increasing Th was seen to have an opposite effect. In both the figures, particles that reach a region close to the leading edge of the boundary layer turn towards the left and exit the domain through the left end of the domain.

Since the particle flow divides into left and right near the leading edge, there exists a saddle point close to the leading edge in the flow field, characterised by zero particle velocity and intersecting particle trajectories.

We obtained such a saddle point in the flow field by solving (2.16) numerically and obtaining the co-ordinates where the particle velocity goes to zero; the intersecting particle trajectories were then obtained by solving (2.16) either backwards in time or forwards in time starting from any point infinitesimally close to the saddle point. Figure 4 shows the obtained particle trajectories close to the saddle point for the case in figure 3(*a*), where the dashed lines show the trajectories of the particles and the solid lines showing the separatrices that pass through the saddle point. At the saddle point, four particle trajectories, two of which end there starting from the top and the bottom of the domain, and two leaving the saddle point towards the left and right so as to exit the domain can be observed in figure 4; we call these trajectories separatrices. For the $Gn = 0$ case shown in figure 4, the separatrix leaving to the right grows in height and forms the boundary of the dust-free region. For the corresponding $Gn = 0.14$ case, as we show later in figure 5, the height of the separatrix leaving to the right would diminish as x increases and the separatrix would eventually touch the plate surface at a finite distance from the origin, making the dust-free region finite in size. For such cases, all trajectories of the particles meet the plate at finite distances from the origin.

The separatrices then divide the flow into four sub regions, labelled as I to IV in figure 4, which are characterised by a different behaviour of particles. In region I, the particles coming down from the top take a right turn and move in the positive x direction. In region II, particles coming down take a left turn and move in the negative x direction. In regions III and IV, the particles close to the plate are lifted off due to the upward component of the thermophoretic force and then take a left or a right turn, respectively. As is clear from the trajectories shown in figure 4, all the particles in regions III and IV either exit from the domain through the right/left or settle on the plate; there is no supply of particles to these regions from the regions I and II on the top. The regions III and IV will hence evolve with time into a dust-free region, with the separatrix AOB as its top boundary; the separatrix AOB is hence the steady-state boundary of the dust-free region close to the hot surface.

3.2. *Particle velocity for small and finite* $\widehat{St}$

For finite but small $\widehat{St}$, for which case the present simulations are conducted, the above flow pattern with saddle point and separatrices can be better understood based on the

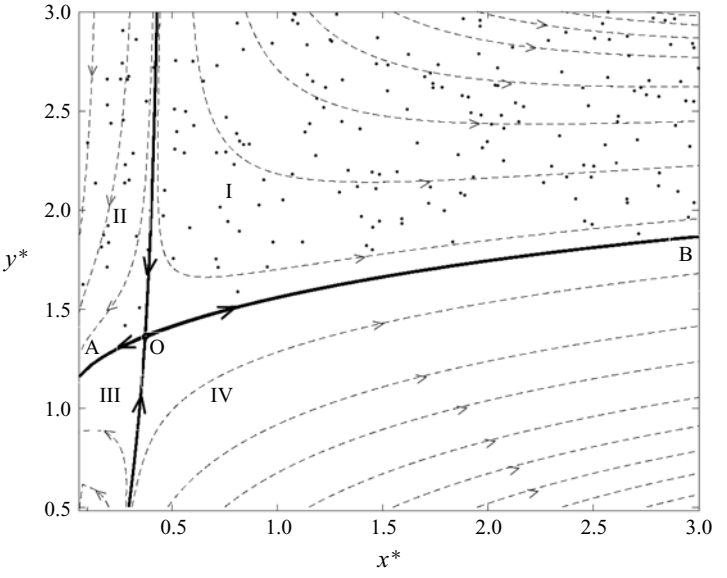

Figure 4. Particle trajectories close to the saddle point for the case shown in figure 3(*a*) with $Gn = 0$ and $Th = 1$. The solid lines show the four separatrices with arrows showing the direction of the particle motion on the separatrix. The dashed lines show the trajectories of the other particles in the flow field. Particle positions in the domain at a later instant after the dust-free region has formed are shown with black dots.

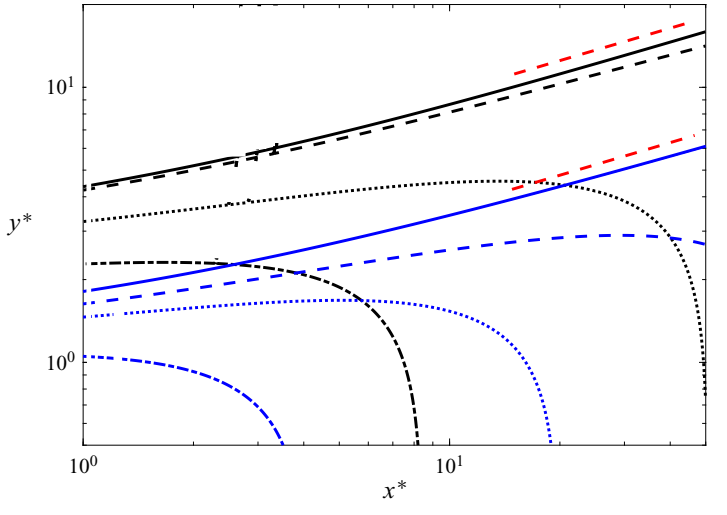

Figure 5. Separatrices for varying ratios of Gn to Th for $Th = 1$ and $Th = 10$ for $\widehat{St} = 10^{-5}$. The blue set of curves corresponds to $Th = 1$ and the black set of curves corresponds to $Th = 10$. ——, $Gn/Th = 0$; – – – –, $Gn/Th = 0.001$; · · · · · ·, $Gn/Th = 0.1$; and -·-·-·-, $Gn/Th = 0.14$. The red dashed lines correspond to $y^* \sim x^{*2/5}$, the scaling of natural convection boundary layer thickness.

simplification of (2.16). For $\widehat{St} \ll 1$, but not equal to zero, (2.18) can be modified as

$$\boldsymbol{v}^* = \boldsymbol{u}^* + \boldsymbol{u}_t^* + \widehat{St}\boldsymbol{a}^*, \tag{3.1}$$

where $\boldsymbol{a}^*$ is an inertial correction that needs to be evaluated. Substituting (3.1) in (2.6), neglecting all terms of order higher than $\widehat{St}$ and then using (2.15), we obtain the inertia corrected particle velocity as

$$\boldsymbol{v}^* = \boldsymbol{u}^* + \boldsymbol{u}_t^* + \boldsymbol{u}_g^* - \widehat{St}\left(\frac{2(1-\epsilon)}{2+\epsilon}\boldsymbol{u}^* \cdot \boldsymbol{\nabla}\boldsymbol{u}^* + \boldsymbol{u}^* \cdot \boldsymbol{\nabla}\boldsymbol{u}_t^* + \boldsymbol{u}_t^* \cdot \boldsymbol{\nabla}\boldsymbol{u}^* + \boldsymbol{u}_t^* \cdot \boldsymbol{\nabla}\boldsymbol{u}_t^*\right). \tag{3.2}$$

Equation (3.2) is a modification of the slow manifold (Sapsis & Haller 2008) of Maxey & Riley (1983) equations with thermophoretic effects. When $\widehat{St} \ll 1$, the last term in (3.2) is negligible while the third term on the right-hand side of (3.2) may still be significant. Hence, for $\widehat{St} \to 0$ but finite, (3.2) simplifies to

$$\boldsymbol{v}^* = \boldsymbol{u}^* + \boldsymbol{u}_t^* + \boldsymbol{u}_g^*, \tag{3.3}$$

implying that the particle velocity will be a superposition of the fluid velocity, the thermophoretic velocity (2.17) and the Stokes settling velocity (2.15).

The presence of a saddle point and separatrices in the flow field can now be better understood in terms of (3.3). Since $\boldsymbol{u}_t^*$ acts opposite to the direction of the temperature gradient, the horizontal and the vertical components of $\boldsymbol{u}_t^*$, namely $u_{t_x}^*$ and $u_{t_y}^*$, expressions for which are derived in Appendix B, will be in the negative x direction and in the positive y direction, respectively. Since the entraining fluid coming down towards the plate takes a turn in the positive x direction inside the boundary layer, the horizontal component u_x^* of the fluid velocity in the boundary layer will be in the positive x direction; u_y^* will be in the negative y direction. Here, $\boldsymbol{u}_g^*$ has only a vertical component in the negative y direction in the case of a horizontal plate. The saddle point is the point where $u_{t_y}^*$ balances u_y^* and u_g^*, as well as where $u_{t_x}^*$ balances u_x^*. Then, in regions I and IV, u_x^* is more than $u_{t_x}^*$, and similarly, in regions II and III, $u_{t_x}^*$ is more than u_x^*. The thermophoretic velocity $\boldsymbol{u}_t^*$ hence balances the components of $\boldsymbol{u}^*$ and $\boldsymbol{u}_g^*$ to create a saddle point, with the four separatrices in the flow field separating regions where the different forces dominate.

Figure 5 shows the plots of separatrices for four different values of Gn/Th at $Th = 1$ and $Th = 10$. As expected, for both values of Th, the areas under the separatrix, which are the dust-free regions, reduce as Gn increases and the gravitational force becomes more dominant. The dust-free region shrinks to a small patch close to the origin of the boundary layer when Gn is of the same order as Th. Figure 5 shows that when $Gn = 0$ or when $Gn \ll Th$, the height of the dust-free region, at distances away from the saddle point, scales as $y^* \sim x^{*2/5}$, shown as the red dashed line, in the same manner as the natural convection boundary layer thickness. However, as is obvious from figure 3(*a*), the thickness of the dust-free region is much lower than the boundary layer thickness. Further, the thickness of the dust-free region is also a function of Th, as shown in figure 5, unlike the boundary layer thickness. As we saw earlier, since the separatrix AOB is the boundary of the dust-free region, an expression obtained for the separatrix would also be an equation for the dust-free region that would expectedly capture the dependence of the dust-free region on the fluid and the flow properties. We now obtain such an expression for the separatrix when the Stokes settling velocity $\boldsymbol{u}_g^* \ll \boldsymbol{u}_t^*$, the thermophoretic velocity, which occurs when $Gn \ll Th$.

The present novel method of finding the dust-free region boundary, by finding the equation for the separatrix, was chosen as earlier proposed conditions to obtain dust-free regions failed in the present situation. Stratmann *et al.* (1988) used the locus of all points having zero vertical velocity as the dust-free region boundary; however, such a curve was observed to be a constant η curve, different from the dust-free region curve, in the

present case. The locus of the maximum negative values of the divergence of the particle velocity field (3.3) was also considered as a criterion to identify the boundary of the dust-free region. This criterion was considered since the particles move out of the dust-free region to the boundary of the dust-free region, and due to its similarity with the recently proposed condition by Shevkar *et al.* (2022) to identify plumes, which are converging flow regions. However, the locus of all such points was found to be another constant η line, which did not coincide with the dust-free region boundary.

3.3. *Scaling of the dust-free region height when $Gn \ll Th$ and $\widehat{St} \ll 1$*

As we saw in § 3.2, when $Gn \ll Th$, the dust-free region height has a similar dependence on x^* as the boundary layer thickness, but which, in contrast to the boundary layer thickness, depends on Th. For such cases, an instance of which is shown in figure 4, we now find an expression for the separatrix AOB; this gives the scaling of the dust-free region height for $Gn \ll Th$. For $\widehat{St} \ll 1$, by taking the ratio of y and x components of (3.3), we obtain a differential equation for the general trajectory of a particle as

$$\frac{\mathrm{d}y^*}{\mathrm{d}x^*} = \frac{v_y^*}{v_x^*} = \frac{u_y^* + u_{t_y}^* + u_g^*}{u_x^* + u_{t_x}^*}. \tag{3.4}$$

From (2.15) and (2.17), u_g^* in (3.4) can be neglected in comparison to $u_{t_y}^*$ since $Gn \ll Th$, to obtain

$$\frac{\mathrm{d}y^*}{\mathrm{d}x^*} \approx \frac{u_y^* + u_{t_y}^*}{u_x^* + u_{t_x}^*}. \tag{3.5}$$

As we saw in § 3, $u_{t_x}^*$ is expected to be smaller than u_x^* in regions I and IV, and hence, also along the separatrix OB. The expressions for u_x^* and $u_{t_x}^*$ given by (2.26) and (B7) further show that for a given Th on constant η line, like the separatrix, $u_{t_x}^*/u_x^* \sim x^{*-6/5}$. Hence, for a given Th far away from O, since the separatrix follows an $\eta =$ constant variation along OB in figure 4, $u_{t_x}^*$ can be neglected in comparison to u_x^*; (3.5) then reduces to

$$\frac{\mathrm{d}y^*}{\mathrm{d}x^*} = \frac{v_y^*}{v_x^*} = \frac{u_y^* + u_{t_y}^*}{u_x^*}. \tag{3.6}$$

Substituting (2.26), (2.27) and (B8) for u_x^*, u_y^* and $u_{t_y}^*$ in (3.6) results in

$$\frac{\mathrm{d}y^*}{\mathrm{d}x^*} = \frac{(-3F(\eta) + 2\eta F'(\eta) - 5ThH'(\eta)Pr^{-1/2})Pr^{1/5}}{5F'(\eta)x^{*3/5}}. \tag{3.7}$$

We now integrate (3.7) with respect to x^* for $\eta =$ constant, a property of the separatrix for $Gn \ll Th$ (see figure 5), to obtain the equation for the separatrix at any Th, when $Gn \ll Th$ and $\widehat{St} \ll 1$, as

$$y^* = \frac{(-3F(\eta) + 2\eta F'(\eta) - 5Pr^{-1/2}ThH'(\eta))x^{*2/5}Pr^{1/5}}{2F'(\eta)}. \tag{3.8}$$

Substituting $\eta = x^{*-2/5}y^*Pr^{-1/5}$ from (B2), (3.8) simplifies to

$$F(\eta) = \frac{-5}{3\sqrt{Pr}}ThH'(\eta), \tag{3.9}$$

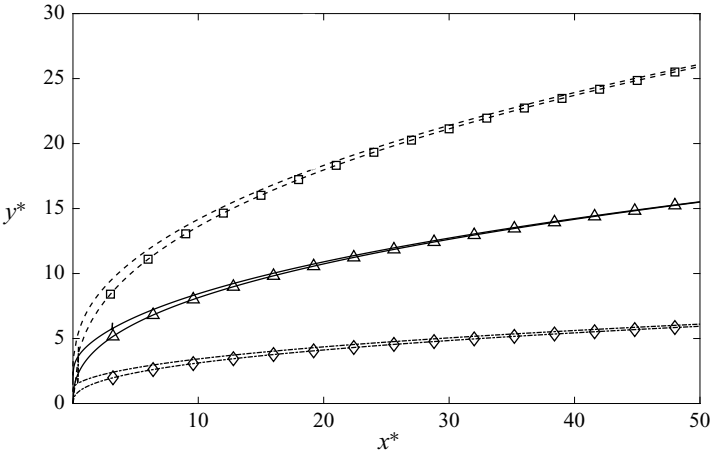

Figure 6. Comparison of separatrices from the numerical solution of (2.16) with the solution of (3.11) for $\widehat{St} = 10^{-5}$, $Gn = 0$ and $Pr = 0.7$, for different Th. Numerical solution of (2.16) for: -·-·-, $Th = 1$; ——, $Th = 10$; – – –, $Th = 100$. The solution of (3.11) for: –◇–, $Th = 1$; –△–, $Th = 10$; –□–, $Th = 100$.

an equation for the separatrix at any Th and Pr when $Gn \ll Th$ and $\widehat{St} \ll 1$. Using the expression for Re from (2.12) in (2.11), and defining a modified thermophoretic number,

$$Th_m = \frac{Th}{\sqrt{Pr}} = \frac{2C_T C_B \Delta T_w}{\langle T \rangle}, \tag{3.10}$$

as a Pr independent dimensionless number for the thermophoretic force, (3.9) can be rewritten as

$$F(\eta) = -\tfrac{5}{3} Th_m H'(\eta). \tag{3.11}$$

Since $F(\eta)$ and $H'(\eta)$ are functions of Pr, the solution of (3.11) will be a function of Th_m and Pr. Using the values of $F(\eta)$ and $H'(\eta)$ obtained from the numerical solution of (2.28*a*) to (2.28*c*) for any Pr, in (3.11), for any given value of Th_m, we get the value of η which specifies the separatrix OB in figure 4, at distances far from the saddle point O. We will hereinafter refer to these values as η_{df}, the subscript df indicating that these curves specify the boundary of the dust-free region. Figure 6 shows the separatrices obtained from the numerical solution of (2.16) for $Th = 1$, $Th = 10$ and $Th = 100$ at $Pr = 0.7$, $Gn = 0$ and $\widehat{St} = 10^{-5}$, along with the η_{df} values predicted by (3.11) for the same values of Th and Pr. It is clear from the figure that the curves of separatrices predicted by (3.11) approximate the dust-free region fairly well in the entire domain, and more accurately, in the regions away from the saddle point. The plots of η_{df} versus Th_m for Pr ranging from 0.1 to 10, obtained from the solution of (3.11), are shown in figure 7. It is observed from the figure that for smaller η_{df} ($\eta_{df} \leq 1$), η_{df} increases as Pr increases while for larger η_{df} ($\eta_{df} \geq 3$), η_{df} decreases as Pr increases. Figure 7 also shows that η_{df} has different scaling dependences on Th_m for small and large η_{df}; we now obtain these scaling laws for small and large η, with the Pr dependence obtained later in § 4.

3.3.1. *Limit* $\eta \to 0$

We obtain the dependence of η_{df} on Th_m for smaller values of η_{df} by using approximations of $F'(\eta)$ and $H(\eta)$ in (3.11) as $\eta \to 0$. A local analysis of (2.28*a*) to (2.28*c*) around $\eta = 0$,

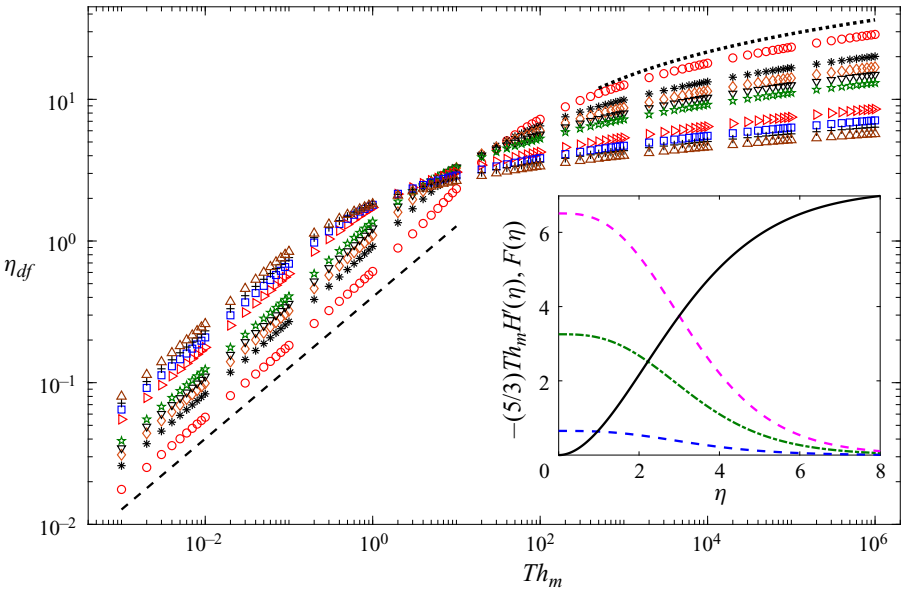

Figure 7. Variation of dimensionless dust-free region height η_{df} with the modified thermophoretic number (3.10) for various Pr: red ○, $Pr = 0.1$; ∗, $Pr = 0.3$; orange ◇, $Pr = 0.5$; ▽, $Pr = 0.7$; green star, $Pr = 1$; red ▷, $Pr = 3$; +, $Pr = 7$; blue □, $Pr = 5$; brown △, $Pr = 10$; – – –, $\eta_{df} \sim \sqrt{Th_m}$; · · · · · · · · ·, $\eta_{df} \sim \ln(Th_m)$. The inset shows the curves $-(5/3)Th_mH'(\eta)$ for; blue – – –, $Th_m = 1$; green – – –, $Th_m = 5$; magenta – – –, $Th_m = 10$; and ——, $F(\eta)$ for $Pr = 0.7$.

given in Appendix C.1, shows that $F'(\eta)$ and $H(\eta)$ are linear functions in η as $\eta \to 0$ (see (C8)). We hence approximate $F'(\eta) = 2M(Pr)\eta$ and $H(\eta) = 1 - N(Pr)\eta$ so that

$$F(\eta) = M(Pr)\eta^2 \tag{3.12a}$$

and

$$H'(\eta) = -N(Pr), \tag{3.12b}$$

where $M(Pr)$ and $N(Pr)$ are some positive real functions of Pr. Using (3.12a) and (3.12b) in (3.11), we obtain

$$\eta_{df} = Q(Pr)\sqrt{Th_m}, \tag{3.13}$$

where using (2.22), (2.23) and (2.3) in (2.21),

$$\eta_{df} = \frac{y_{df}}{(Z_w^3 x^2 Pr)^{1/5}} \tag{3.14}$$

is the dimensionless dust-free region height, with y_{df} being the dimensional dust-free region height and

$$Q(Pr) = \sqrt{\frac{5}{3}\frac{N(Pr)}{M(Pr)}} \tag{3.15}$$

is a function of $N(Pr)$ and $M(Pr)$. Since both $N(Pr)$ and $M(Pr)$ are positive real functions, $Q(Pr)$ is always positive for a hot plate, because of which, for all Pr, η_{df} always increase as $\sqrt{Th_m}$ for small η, as shown in figure 7.

3.3.2. *Limit* $\eta \to \infty$

The dependence of η_{df} on Th_m for large values of η_{df} is obtained as follows. As $\eta \to \infty$, the boundary condition (2.30*b*) implies that

$$F(\eta) = C_1(Pr), \tag{3.16a}$$

where $C_1(Pr)$ is a positive real function of Pr. Using (3.16*a*) in (2.28*c*) and then integrating gives

$$H'(\eta) = C_2(Pr)\, \mathrm{e}^{-3C_1(Pr)Pr\eta/5}, \tag{3.16b}$$

where $C_2(Pr)$ is a negative real function of Pr. Using (3.16*a*) and (3.16*b*) in (3.11) gives

$$\eta_{df} = R(Pr) + S(Pr)\ln(Th_m), \tag{3.17}$$

where

$$R(Pr) = \frac{-5}{3PrC_1(Pr)} \ln\left(\frac{-3C_1(Pr)}{5C_2(Pr)}\right) \quad \text{and} \quad S(Pr) = \frac{5}{3}\frac{1}{C_1(Pr)Pr} \tag{3.18a,b}$$

are functions of Pr. Since $S(Pr)$ is a positive real function in Pr, we see that η_{df} increases as $\ln(Th_m)$ for all Pr at large η as shown in figure 7; a higher η_{df} always corresponds to a higher value of Th_m for a given Pr. This dependence could also be explained from a graphical depiction of (3.11). The inset of figure 7 shows a plot of $-(5/3)Th_mH'(\eta)$, the right-hand side of (3.11), versus η for $Pr = 0.7$ along with the plot for $F(\eta)$, the left-hand side of (3.11), versus η for the same Pr. The curves for $-(5/3)Th_mH'(\eta)$ corresponding to $Th_m = 1$, $Th_m = 5$ and $Th_m = 10$ cross the curve for $F(\eta)$ at higher values of η, as Th_m is increased from 1 to 10. In (3.13) and (3.17), the Pr dependence of η_{df} is not fully specified; we now obtain the complete expressions for η_{df} in terms of Pr and Th_m for different ranges of Pr.

4. Scaling laws for dust-free region heights

The velocity function F' and the temperature function H in the boundary layer equations (2.28) uncouple for $Pr \to 0$ and $Pr \to \infty$. This, however, occurs since (2.28*a–c*) are not valid for these asymptotic Pr cases. When $Pr \gg 1$, the thermal boundary layer thickness is much smaller than the velocity boundary layer thickness; the opposite occurs when $Pr \ll 1$. Rotem & Claassen (1969) treats these two asymptotic Pr cases as two separate boundary layer problems. They solve a set of inner boundary layer equations for the thin boundary layer inside, and a set of outer boundary layer equations for the larger boundary layer region outside; we follow the same approach to obtain scaling laws for η_{df} for $Pr \ll 1$ and $Pr \gg 1$. Hereinafter, we use the subscripts 1 and 2 to denote the inner and outer boundary layer parameters, and a single tilde and a double tilde to denote the $Pr \gg 1$ and the $Pr \ll 1$ cases, respectively. A brief explanation of the stretched variables used by Rotem & Claassen (1969) in these regimes of Pr is provided in Appendix D.

4.1. *Scaling for* $Pr \gg 1$

4.1.1. *Scaling for small* η

Rotem & Claassen (1969) provides the inner boundary layer equations for the case of $Pr \gg 1$ as follows:

$$5\tilde{F}_1''' = 2\tilde{G}_1 - 2\tilde{\eta}\tilde{G}_1', \quad \tilde{H}_1 = \tilde{G}_1', \quad \tilde{H}_1'' + \tfrac{3}{5}\tilde{F}_1\tilde{H}_1' = 0, \tag{4.1a–c}$$

where $\tilde{F}_1$, $\tilde{G}_1$ and $\tilde{H}_1$ are the dimensionless velocity, pressure and temperature functions obtained by using appropriate transformations as in (D6) and (D7). The boundary

conditions include

$$\tilde{F}_1 = \tilde{F}_1' = 0; \quad \tilde{H}_1 = \tilde{G}_1' = 1 \quad \text{at } \tilde{\eta}_1 = 0 \tag{4.2a}$$

and

$$\tilde{F}_1'' = 0; \quad \tilde{H}_1 = \tilde{G}_1 = 0 \quad \text{when } \tilde{\eta}_1 \to \infty, \tag{4.2b}$$

where $\tilde{\eta}_1$ is the similarity variable defined for $Pr \gg 1$ in (D6). Since there is no Pr appearing in (4.1), $\tilde{F}_1$ and $\tilde{H}_1$ will only depend of $\tilde{\eta}_1$ and not on Pr.

A local analysis of (4.1) near $\tilde{\eta}_1 = 0$, given in Appendix C.2, shows that $\tilde{F}_1'(\tilde{\eta}_1)$ and $\tilde{H}_1(\tilde{\eta}_1)$ are linear when $\tilde{\eta}_1 \to 0$. In such a case,

$$\tilde{F}_1(\tilde{\eta}_1) = C_1 \tilde{\eta}_1^2, \tag{4.3}$$

where $C_1 = \tilde{F}_1''(\tilde{\eta}_1 = 0)/2 = 0.49$ and

$$\tilde{H}_1'(\tilde{\eta}_1) = C_2, \tag{4.4}$$

where $C_2 = \tilde{H}_1'(0) = -0.46$. It is to be noted that $\tilde{F}_1(\tilde{\eta}_1)$ in (4.3) and $\tilde{H}_1'(\tilde{\eta}_1)$ in (4.4) are independent of Pr, since the boundary layer equations (4.1) do not have Pr in them. So C_1 and C_2 are just constants and not functions of Pr. From (D9), (D3) and (D5*b*), we have

$$F'(\eta) = Pr^{-3/5} \tilde{F}_1'(\tilde{\eta}_1). \tag{4.5}$$

Similarly, from (D5*a*), (D6*c*) and (2.21), we obtain

$$\eta = Pr^{-1/5} \tilde{\eta}_1. \tag{4.6}$$

Using (4.6) in (4.5) and integrating, since $\tilde{F}_1(0)$ and $F(0)$ are equal to zero gives us

$$F(\eta) = Pr^{-4/5} \tilde{F}_1(\tilde{\eta}_1). \tag{4.7}$$

Differentiating (D6*b*) and using (4.6), we get

$$H'(\eta) = Pr^{1/5} \tilde{H}_1'(\tilde{\eta}_1). \tag{4.8}$$

Even though both $\tilde{F}_1(\tilde{\eta}_1)$ and $\tilde{H}_1'(\tilde{\eta}_1)$ are independent of Pr (see (4.3) and (4.4)), the transformation back to the original boundary layer variables $F(\eta)$ and $H'(\eta)$ in (4.7) and (4.8) brings back the Pr dependence of the velocity and the temperature fields. Using (4.7) and (4.8) to convert (4.3) and (4.4) to be in terms of η, then substituting in (3.11) and using (4.6), we get

$$\eta_{df} = 1.25\sqrt{Th_m} Pr^{3/10}. \tag{4.9}$$

Equation (4.9) is the theoretically obtained scaling relation for η_{df} in the small η limit for $Pr \gg 1$. A comparison of (3.13) with (4.9) makes it clear that the unspecified Pr dependence in (3.13) is

$$Q(Pr) = 1.25 Pr^{3/10}. \tag{4.10}$$

In figure 8, we compare (4.9) with η_{df} obtained from (3.11) for $Pr = 2$, $Pr = 10$ and $Pr = 100$; where $F(\eta)$ and $H'(\eta)$ corresponding to $Pr = 2$, $Pr = 10$ and $Pr = 100$ used in (3.11) were obtained by numerically solving (2.28). Since (4.9) is valid for $Pr \gg 1$, we expect the data of $Pr = 100$ to approach (4.9) in the small η limit, while the data of $Pr = 2$ to deviate. Surprisingly, in figure 8, the data of $Pr = 2$, $Pr = 10$ and $Pr = 100$ collapse onto (4.9) suggesting that (4.9) is valid not just for $Pr \gg 1$, but also for any $Pr > 1$, for small η.

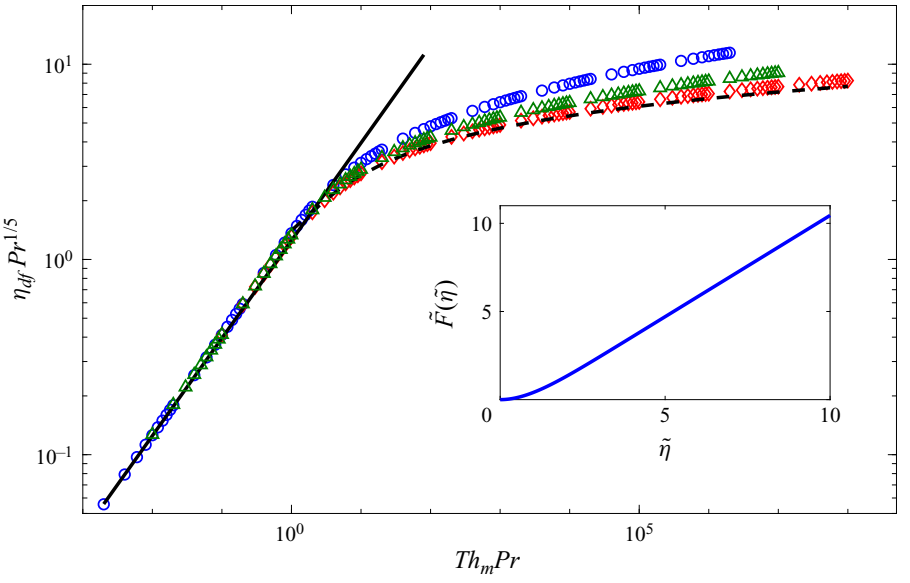

Figure 8. Scaling of the dimensionless dust-free region height η_{df} for $Pr \gg 1$ in the small and the large η limits. Numerical solution of (3.11) for: blue ○, $Pr = 2$; green △, $Pr = 10$; and red ◇, $Pr = 100$. The scaling relations ———, (4.9) and – – – –, (4.13). The inset shows the variation of $\tilde{F}(\tilde{\eta})$ with $\tilde{\eta}$ for $Pr \gg 1$, obtained by solving the inner boundary layer equations (4.1).

4.1.2. *Scaling for large η*

For $Pr \gg 1$, the thermal boundary layer is an inner boundary layer; there is negligible temperature gradient above it in the velocity boundary layer. Since thermophoresis and the resultant formation of the dust-free region are due to temperature gradients, for $Pr \gg 1$, we expect the dust-free region to not extend beyond this inner thermal boundary layer. The scaling of the dust-free region height in the large η limit has to be then obtained from an analysis of the top regions of the inner thermal boundary layer. We hence look at the inner boundary layer equations (4.1), with the corresponding boundary conditions (4.2) to find the large η scaling of η_{df} at $Pr \gg 1$.

From the $\tilde{\eta}_1 \to \infty$ boundary condition for the velocity function in (4.2*b*), we find that $\tilde{F}_1$ should be varying linearly as

$$\tilde{F}_1(\tilde{\eta}_1) = -C_3 + C_4 \tilde{\eta}_1. \tag{4.11}$$

This linear variation of $\tilde{F}_1$ for large $\tilde{\eta}_1$ can be seen in the inset of figure 8, which shows the variation of $\tilde{F}_1(\tilde{\eta}_1)$ with $\tilde{\eta}_1$ obtained by solving (4.1). We obtain $C_3 = 1.04$ and $C_4 = 1.15$ from the y intercept and the slope of the linear portion of this plot. Substituting (4.11) in (4.1*c*) and integrating gives us $\tilde{H}_1'(\tilde{\eta}_1)$ at large $\tilde{\eta}_1$ as

$$\tilde{H}'(\tilde{\eta}) = C_5 \, \mathrm{e}^{-3C_4(\tilde{\eta} - C_3/C_4)^2/10}. \tag{4.12}$$

A curve fit to the values of $\tilde{H}'(\tilde{\eta})$ for $Pr \gg 1$, obtained by numerically solving (4.1), showed that $C_5 = -0.38$. Converting (4.11) and (4.12) into $F(\eta)$ and $H'(\eta)$ by using (4.7) and (4.8), and then substituting in (3.11) and using (4.6), we get

$$\eta_{df} Pr^{1/5} = 0.90 + \sqrt{1.45 W_0(0.21 (Th_m Pr)^2)}, \tag{4.13}$$

where $W_0(x)$ is the Lambert W function, which is the inverse function of $y\,\mathrm{e}^y = x$.

Equation (4.13) is the expression for η_{df} in the large η limit for $Pr \gg 1$. In figure 8, we compare (4.13) with η_{df} obtained from (3.11) for $Pr = 2$, $Pr = 10$ and $Pr = 100$, where the $F(\eta)$ and the $H'(\eta)$ corresponding to $Pr = 2$, $Pr = 10$ and $Pr = 100$ used in (3.11) were obtained by numerically solving (2.28). As expected, the data of $Pr = 100$ are very close to the curve of (4.13), which was derived for the limit of $Pr \gg 1$, while the data of $Pr = 2$ deviate from (4.13). Thus, (4.13) seems to hold as an analytic expression for the dust-free region height for $Pr \geq 100$ for large η_{df} values corresponding to higher Th_m. We now examine the scaling laws for the large and the small η cases for low Pr.

4.2. *Scaling for $Pr \ll 1$*

4.2.1. *Scaling for large η*

For $Pr \ll 1$, Rotem & Claassen (1969) gives the outer boundary layer equations in terms of the dimensionless velocity $\tilde{\tilde{F}}_2$ in (D12*a*), pressure $\tilde{\tilde{G}}_2$ in (D13) and temperature function $\tilde{\tilde{H}}_2$ in (D12*b*) in the outer boundary layer as

$$3\tilde{\tilde{F}}_2\tilde{\tilde{F}}_2'' - (\tilde{\tilde{F}}_2')^2 = 2\tilde{\tilde{G}}_2 - 2\tilde{\tilde{\eta}}_2\tilde{\tilde{G}}_2', \quad \tilde{\tilde{H}}_2 = \tilde{\tilde{G}}_2', \quad \tilde{\tilde{H}}_2'' + \frac{3}{5}\tilde{\tilde{F}}_2\tilde{\tilde{H}}_2' = 0, \tag{4.14a–c}$$

with the boundary conditions

$$\tilde{\tilde{F}}_2 = 0, \quad \tilde{\tilde{H}}_2 = \tilde{\tilde{G}}_2' = 1 \quad \text{at } \tilde{\tilde{\eta}}_2 = 0 \tag{4.15a}$$

and

$$\tilde{\tilde{F}}_2' = 0, \quad \tilde{\tilde{H}}_2 = \tilde{\tilde{G}}_2 = 0 \quad \text{when } \tilde{\tilde{\eta}}_2 \to \infty. \tag{4.15b}$$

The subscript 2 in the above equations is for the outer boundary layer.

From (D15), (D3) and (D11*c*), we have

$$F'(\eta) = Pr^{-1/5}\tilde{\tilde{F}}_2'(\tilde{\tilde{\eta}}_2). \tag{4.16}$$

Similarly, we have

$$\eta = Pr^{-2/5}\tilde{\tilde{\eta}}_2 \tag{4.17}$$

from (D11*a*), (D11*b*), (D12*c*) and (2.21). Using (4.17) in (4.16), integrating, and since $F(0)$ and $\tilde{\tilde{F}}_2(0)$ are equal to zero from (2.30*a*) and (4.15*a*), respectively, we get

$$F(\eta) = Pr^{-3/5}\tilde{\tilde{F}}_2(\tilde{\tilde{\eta}}_2). \tag{4.18}$$

Differentiating (D12*b*) and using (2.20) and (4.17), we get

$$H'(\eta) = Pr^{2/5}\tilde{\tilde{H}}_2'(\tilde{\tilde{\eta}}_2). \tag{4.19}$$

From the boundary condition for velocity function in (4.15*b*) for $\tilde{\tilde{\eta}}_2 \to \infty$, we see that

$$\tilde{\tilde{F}}_2(\tilde{\tilde{\eta}}_2) = C_6, \tag{4.20}$$

where the constant $C_6 = 1.78$ is obtained from the numerical solution of (4.14). Using (4.20) in (4.1*c*) and integrating gives

$$\tilde{\tilde{H}}_2'(\tilde{\tilde{\eta}}_2) = C_7\, \mathrm{e}^{-3C_6\tilde{\tilde{\eta}}_2/5}, \tag{4.21}$$

where $C_7 = -1.97$, as obtained by numerically solving (4.14) for $\tilde{\tilde{H}}_2'(\tilde{\tilde{\eta}}_2)$.

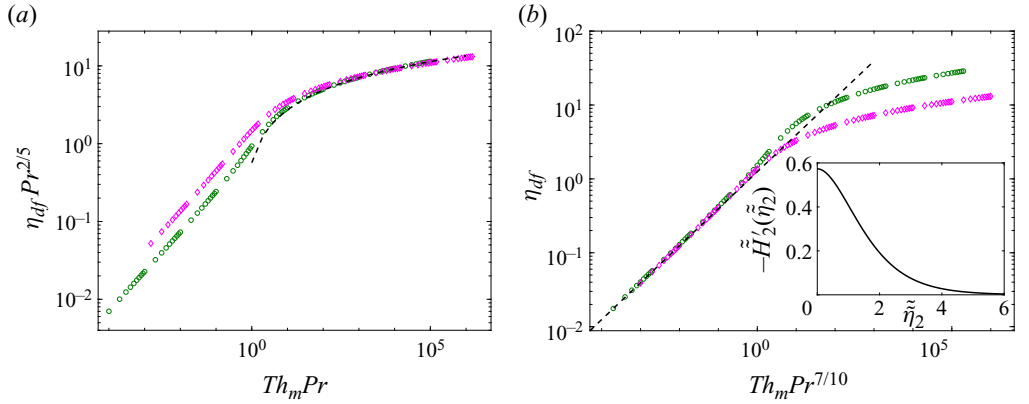

Figure 9. Scaling of the dimensionless dust-free region height (η_{df}) at $Pr \ll 1$ in the large and the small η limits. (*a*) Large η limit. Numerical solutions at green ○, $Pr = 0.1$ and magenta ◇, $Pr = 1$; −−−−, scaling relation (4.22). (*b*) Small η limit. Numerical solutions at green ○, $Pr = 0.1$ and magenta ◇, $Pr = 1$; −−−−, scaling relation (4.29). The inset shows the variation of $\tilde{\tilde{H}}_2'(\tilde{\tilde{\eta}})$ with $\tilde{\tilde{\eta}}$ for $Pr \ll 1$, obtained by solving the outer boundary layer equations (4.14).

Using (4.17), (4.18) and (4.19) to convert (4.20) and (4.21) to be in terms of η, and then substituting in (3.11), we get the dimensionless dust-free region height at large η for $Pr \ll 1$ as

$$\eta_{df} = 0.93 Pr^{-2/5} \ln(1.84 Th_m Pr). \tag{4.22}$$

In figure 9(*a*), we compare (4.22) with the η_{df} obtained from (3.11) by using the numerical solution of (2.28) for $Pr = 0.1$ and $Pr = 1$. Since (4.22) was obtained from the equations of Rotem & Claassen (1969) for $Pr \ll 1$ in (4.14), as expected, the numerical solution for $Pr = 0.1$ agrees with the scaling relation (4.22) for large η. However, surprisingly, the data for $Pr = 1$ also match with (4.22) for large η, suggesting that (4.22) is valid even for $Pr \leq 1$. Thus, (4.22) gives the scaling for the dimensionless dust-free region height for $Pr \leq 1$ for large Th_m.

4.2.2. *Scaling for small η*

Rotem & Claassen (1969) provides the inner boundary layer equations for $Pr \ll 1$ as

$$5\tilde{\tilde{F}}_1''' + 3\tilde{\tilde{F}}_1\tilde{\tilde{F}}_1'' - \tilde{\tilde{F}}_1'^2 = -1, \quad \tilde{\tilde{H}}_1 = 1, \tag{4.23a,b}$$

subjected to the boundary conditions,

$$\tilde{\tilde{F}}_1 = \tilde{\tilde{F}}_1' = 0 \quad \text{at } \tilde{\tilde{\eta}}_1 = 0 \tag{4.24a}$$

and

$$\tilde{\tilde{F}}_1' = 1 \quad \text{when } \tilde{\tilde{\eta}}_1 \to \infty. \tag{4.24b}$$

Subscript 1 in the above equations denote the inner boundary layer. However, (4.23*b*) implies that the temperature gradient inside the inner velocity boundary layer, $\tilde{\tilde{H}}_1' = 0$; this is quite unphysical since the maximum temperature gradient in natural convection flows occurs at the wall. So we assume that the temperature gradient in the outer velocity boundary layer, which approaches a constant value at lower $\tilde{\tilde{\eta}}_2$, is maintained throughout

the inner thermal boundary layer. By numerically solving the set of outer boundary layer equations (4.14), we get

$$\tilde{\tilde{H}}_2'(\tilde{\tilde{\eta}}_2) = C_8 = -0.57, \tag{4.25}$$

as $\tilde{\tilde{\eta}}_2 \to 0$, shown as the y-intercept in the inset of figure 9(b). From a local analysis of (4.23) near $\tilde{\tilde{\eta}}_1 = 0$, given in Appendix C.3, we see that $\tilde{\tilde{F}}_1$ can be approximated to

$$\tilde{\tilde{F}}_1(\tilde{\tilde{\eta}}_1) = C_9 \tilde{\tilde{\eta}}_1^{\,2}. \tag{4.26}$$

As given by Rotem & Claassen (1969),

$$F(\eta) = Pr^{-1/10} \sqrt{\tilde{\tilde{F}}_2'(0)}\, \tilde{\tilde{F}}_1(\tilde{\tilde{\eta}}_1) \tag{4.27}$$

and

$$\eta = \frac{Pr^{1/10} \tilde{\tilde{\eta}}_1}{\sqrt{\tilde{\tilde{F}}_2'(0)}}. \tag{4.28}$$

Using (4.27) to convert (4.26) into $F(\eta)$, (4.19) to convert (4.25) into $H'(\eta)$, substituting these in (3.11), and using (4.28), we get

$$\eta_{df} = 1.75 Pr^{7/20} Th_m^{1/2} \tag{4.29}$$

as the scaling law to predict η_{df} for $Pr \ll 1$ in the small η limit. Here, the pre-factor 1.75 is chosen to match (4.29) with the data from the solution of (3.11) for $Pr < 1$, plotted in figure 9(b). Figure 9(b) shows the comparison of (4.29) with the dust-free region height obtained from the numerical solutions of (3.11) for $Pr = 0.1$ and $Pr = 1$. We again note from the figure that (4.29) is valid for any $Pr \leq 1$, even though it was derived for $Pr \ll 1$.

4.2.3. *Large η scaling for intermediate Pr ($1 < Pr < 10$)*

We saw in §§ 4.1.1 and 4.2.2 that the scaling laws for the dust-free region heights obtained in the small η limit for $Pr \gg 1$ in (4.9) and for $Pr \ll 1$ in (4.29) are valid for any $Pr > 1$ and $Pr < 1$. Similarly, the scaling law for the large η limit for $Pr \ll 1$ in (4.22) was shown to be valid for any $Pr < 1$. However, the scaling law in the large η limit for $Pr \gg 1$ in (4.13) deviates from the simulation data for $Pr = 2$ (see figure 8). Then in the intermediate range of Pr values which are not much larger than one, for large Th_m that push the η_{df} to large η limits, the prediction of η_{df} becomes difficult with the results presented so far. To overcome this limitation, we now obtain an expression, by trial and error using numerical solutions of $F(\eta)$ and $H'(\eta)$ obtained from (2.28), which collapse the η_{df} data from the solutions of (3.11) for $1 < Pr < 10$. A logarithmic function,

$$\eta_{df} Pr^{0.39} = 0.68 \ln(41.2 Th_m Pr^{1.5}), \tag{4.30}$$

and the corresponding data from the solution of (3.11) are compared in figure 10 for the large η limit for $2 < Pr < 10$; the data of simulations collapse on to (4.30) fairly well for this range of intermediate Pr.

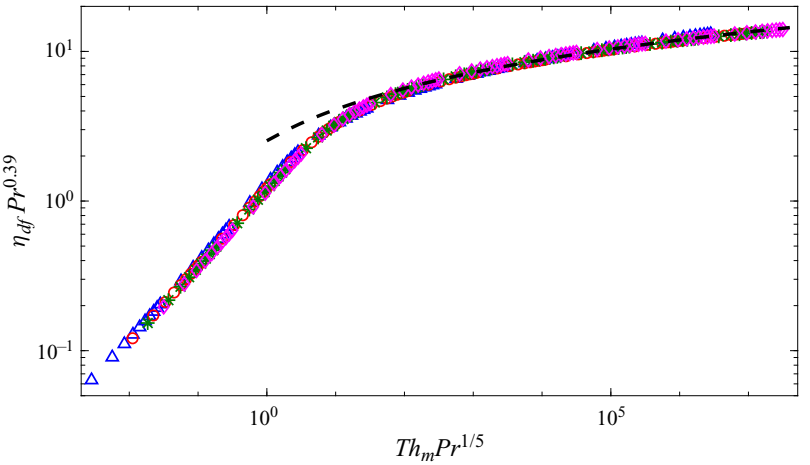

Figure 10. Comparison of the scaling of the dimensionless dust-free region height for $1 < Pr < 10$ with η_{df} obtained from the numerical solution; blue $\triangle$, $Pr = 2$; red $\circ$, $Pr = 5$; green $*$, $Pr = 7$; magenta $\diamond$, $Pr = 10$; ----, (4.30).

5. Conclusions

The primary contribution of the present work includes the identification of a saddle point and a separatrix for particle flows inside natural convection boundary layers over horizontal surfaces and the scaling of the dust-free region boundary in such flows for the whole range of Prandtl numbers, $Pr \ll 1$ to $Pr \gg 1$. The saddle point and the separatrix were identified by studying the particle trajectories obtained by simulating the motion of low-Stokes-number ($\widehat{St}$ (2.8)) particles in the flow field of laminar natural convection boundary layer given by Rotem & Claassen (1969), by including thermophoretic force, particle inertia, viscous drag and gravitational force. The saddle point and the four separatrices that originate from it were shown to divide the flow field of particles into four regions. The regions below the two separatrices leaving the saddle point always turned into a dust-free zone. For a given fluid and flow conditions, the size of this zone was shown to depend on the gravitational number, Gn in (2.13), and the thermophoretic number, Th in (2.11), when $\widehat{St} \ll 1$ and Brownian effects were not significant. The size of the dust-free zone was shown to decrease with an increase in Gn and diminish to zero when $Gn \gg Th_m$.

For small particle sizes and appreciable temperature differences across the boundary layer, so that $\widehat{St} \ll 1$ and $Gn \ll Th$, the boundary of the dust-free region was shown to be parallel to the boundary layer edge, but smaller in height and dependent on the values of Th and Pr. For such commonly occurring conditions, since the separatrix formed the boundary of the dust-free region, by considering the dominant velocity components on the separatrix, we obtained a differential equation (3.7) for the particle trajectory on these separatrices, and from which, an equation (3.11) for the dimensionless boundary layer y-coordinate (η_{df}) associated with the separatrix. This equation showed that on the separatrix, which is the boundary of the dust-free region, the dimensionless stream function $F(\eta)$ in (2.19) is proportional to the dimensionless derivative $(\partial/\partial\eta)$ of the dimensionless temperature function $H(\eta)$ in (2.20); the proportionality coefficient being $-(5/3)(Th/\sqrt{Pr})$. The numerical solution of this equation was shown to predict the dust-free regions very well at all locations of the boundary layer, except for a slight deviation close to the leading edge. However, (3.11) was not an equation that gave an

explicit scaling relation for the dimensionless dust-free region boundary η_{df}; further, the solution of it required the similarity solutions of the boundary layer equations, corresponding to each Pr.

Using the limiting forms of $F(\eta)$ and $H(\eta)$ for $\eta \ll 1$, which implied small Th, in (3.11) for the dimensionless dust-free region height, $\eta_{df} = y_{df}/[Pr(x^2 Z_w^3)^{1/5}]$, where Z_w(2.3) is the near wall length scale in turbulent convection, we then obtained the scaling of dust-free region heights. In both the Pr cases, η_{df} scaled as $\sqrt{Th_m}$, with the Pr dependence being $Pr^{3/10}$ for $Pr \gg 1$ and $Pr^{7/20}$ for $Pr \ll 1$ (see (4.9) and (4.29)). For the large η cases, η_{df} had a more complex dependence for large and small Pr; η_{df} showed a dependence on the square root of the Lambert function of $Th^2 Pr$ (see (4.13)) for $Pr \gg 1$ and a dependence on the logarithm of $Th\sqrt{Pr}$ for $Pr \ll 1$ (see (4.22)). All of these scalings matched well with the numerical solution of (3.11) even for the corresponding $Pr \leq 1$ and $Pr \geq 1$ cases, except for the $Pr \gg 1$, $\eta \gg 1$ scaling in (4.13), which matched with (3.11) only for $Pr \geq 100$. A scaling for η_{df} in the practically relevant regime of $1 < Pr < 10$ for $\eta \gg 1$ is then empirically obtained as $\eta_{df} \sim Pr^{-0.39} \ln(Th_m Pr)$ (see (4.30)) so as to obtain the scaling of the dust-free region in the whole range of $Pr \ll 1$ to $Pr \gg 1$.

The present study neglected Brownian effects, which become important with the decrease in the size of the particles. Brownian effects on the particles depend just on the absolute value of the temperature, whereas thermophoretic effects depend on the gradient of temperature across particles, which keeps increasing as we move towards the origin of the boundary layer. So, even in the presence of Brownian effects, we still expect the presence of a similar dust-free region above a hot horizontal plate. As the Brownian effects increase, one may expect the height of the dust-free region to decrease, finally making it bounded, as we had observed in the gravitational case. A further increase in Brownian effects may reduce the dust-free region size close to zero and confine it around the leading edge of the boundary layer. These effects, and the similarities that the dust-free region may show in such cases to the case when gravitational effects are increased, need to be investigated.

As we saw earlier, since at intermediate Ra the local boundary layers on either side of the plumes in Rayleigh–Bénard convection could be modelled as a laminar natural convection boundary layer (Theerthan & Arakeri 1998; Puthenveettil 2004; Puthenveettil & Arakeri 2005) the dust-free region heights predicted by the present study could be expected to occur near the hot plate in Rayleigh–Bénard convection at intermediate Ra. The upper limit for Ra is discussed in Appendix E in detail for $Pr = 0.7$ and aspect ratio of 1. However, when Ra is higher, these local boundary layers are sheared by the large-scale flow in the bulk, changing their nature to mixed convection boundary layers (Shevkar, Mohanan & Puthenveettil 2023). Hence, the results of the present study may not be valid for high-Ra Rayleigh–Bénard convection, even though the local boundary layers remain.

Supplementary movies. Supplementary movies are available at https://doi.org/10.1017/jfm.2024.786.

Acknowledgements. The authors would like to acknowledge the partial financial support from DST, Government of India under the Core research grant CRG/2021/007497 and the FIST grants SR/FST/ETII-017/2003; SR/FST/ETII-064/2015 for this study.

Declaration of interests. The authors report no conflict of interest.

Author ORCIDs.
K.K. Prasoon https://orcid.org/0009-0000-3128-9140;
Anubhab Roy https://orcid.org/0000-0002-0049-2653;
Baburaj A. Puthenveettil https://orcid.org/0000-0002-8694-4322.

Appendix A. Dilute mixture assumption

The present study is done for $\widehat{St} = 10^{-5}$ with the number of particles $N = 5000$ in a domain of $H = 40Z_w$ and $L = 50Z_w$. The area fraction that N particles of radius a occupy is then

$$\phi = \frac{N\pi a^2}{40Z_w 50Z_w}. \tag{A1}$$

Since

$$Z_w = \frac{2^{1/3}H}{Ra_H^{1/3}}, \tag{A2}$$

where

$$Ra_H = \frac{g\beta\Delta T H^3}{\nu\alpha} \tag{A3}$$

is the Rayleigh number, (A1) can be written as

$$\phi = \frac{N\pi}{2^{5/3}\times 10^3}\left(\frac{a}{H}\right)^2 Ra_H^{2/3}. \tag{A4}$$

Using the expression for (2.8), (2.9) and (A2), for $\widehat{St} = 10^{-5}$,

$$\frac{a}{H} = \left(\frac{2^{4/3}\times 40^2\times 10^{-5}\times 9}{C_B}\frac{\epsilon}{2+\epsilon}\right)^{1/2}\frac{Pr^{1/4}}{Ra_H^{2/3}}. \tag{A5}$$

Substituting (A5) in (A4), we obtain

$$\phi = \frac{N\times 3.6\times 10^{-4}}{C_B}\frac{\epsilon}{2+\epsilon}\frac{\sqrt{Pr}}{Ra_H^{2/3}}. \tag{A6}$$

The dilute mixture assumption is valid for $\phi \ll 1$. Using the values of $N = 5000$, $Pr = 0.7$ and $C_B \simeq 1$ for particles in air, with $\epsilon/(2+\epsilon) \to 1/2$ when $\epsilon \to 0$ for particles in air, we obtain

$$\phi = \frac{0.75}{Ra_H^{2/3}}. \tag{A7}$$

For the usual range of $Ra_H > 10^6$, for which boundary layers form on the hot plate, $\phi < 7.5\times 10^{-5} \ll 1$; the influence of particles on the flow field can then be ignored.

Appendix B. Dimensionless stream function and thermophoretic velocity

In this section, we derive expressions for the dimensionless stream function used to obtain u_x^* and u_y^* in (2.26) and (2.27) and the dimensionless thermophoretic velocity components, $u_{t_x}^*$ and $u_{t_y}^*$, used in (3.5).

B.1. *Dimensionless stream function*

Using (2.3) and (2.24), we get

$$Gr = \left(\frac{L}{Z_w}\right)^3 \frac{1}{Pr}. \tag{B1}$$

Substituting (B1) and (2.3) in (2.21), we get

$$\eta = Pr^{-1/5} x^{*-2/5} y^*. \tag{B2}$$

The dimensionless stream function, ψ^* in (2.19), can now be expressed in terms of x^* by using (2.3), (2.22) and (B1) as

$$\psi^* = Pr^{-1/5} Gr^{-1/5} x^{*3/5} F(\eta). \tag{B3}$$

The dimensionless fluid velocity components $u_x^* = \partial\psi^*/\partial\hat{y}$ in (2.26) and $u_y^* = -\partial\psi^*/\partial {x_{rc}}^*$ in (2.27) can now be obtained from (B3). Since $F'(\eta)$ is always positive (see figure 2), it is clear from (2.26) that the horizontal component of fluid velocity, u_x^* is always positive. Equations (2.26) and (2.27) imply that along any constant η lines, u_x^* monotonically increases with increase in x^*, while the magnitude of vertical velocity, u_y^*, decreases with increase in x^*.

B.2. *Dimensionless thermophoretic velocity components*

Using (2.12) in (2.17), we can re-write the dimensionless thermophoretic velocity as

$$\boldsymbol{u}_t^* = -2\sqrt{Pr} C_T C_B \frac{\Delta T_w}{\langle T \rangle} \nabla^* \theta. \tag{B4}$$

Comparing (2.17) and (B4), the thermophoretic number can be written as

$$Th = 2\sqrt{Pr} C_T C_B \frac{\Delta T_w}{\langle T \rangle}. \tag{B5}$$

Using

$$\boldsymbol{\nabla}^* \theta(\eta) = \theta'(\eta) \boldsymbol{\nabla}^* \eta, \tag{B6}$$

(B2), (B5) and (2.20) in (B4), the horizontal component of thermophoretic velocity becomes

$$u_{t_x}^* = \tfrac{2}{5} x^{*-1} \eta Th H'(\eta). \tag{B7}$$

Similarly, the vertical component of the thermophoretic velocity can be written as

$$u_{t_y}^* = -Th Pr^{-1/5} x^{*-2/5} H'(\eta). \tag{B8}$$

Note that $u_{t_x}^*$ is always negative and $u_{t_y}^*$ is always positive as H' is always negative (see figure 2). It is also evident from (B7) and (B8) that the magnitudes of $u_{t_x}^*$ and $u_{t_y}^*$ decrease as x^* increases along any constant η lines.

Appendix C. Limiting behaviours of dimensionless stream, temperature and pressure functions for $\eta \to 0$

C.1. *For* $0.1 \leq Pr \leq 10$, *behaviour of* $F(\eta)$, $G(\eta)$ *and* $H(\eta)$ *near* $\eta = 0$

For small values of η, a first-order approximation to $F(\eta)$ (see figure 2) can be made as

$$F(\eta) \approx A\eta^{\alpha}, \tag{C1}$$

where the coefficient A and the exponent α are real numbers. The higher order terms in η can be neglected as $\eta \to 0$. This approximation ensures that both $F(\eta)$ and $F'(\eta)$ go to zero (see boundary conditions in (2.30*a*)) as $\eta \to 0$ when α is greater than one. Similarly, a first-order approximation of the decreasing function $H(\eta)$ (see figure 2) can be made as

$$H(\eta) \approx 1 - B\eta^{\beta}, \tag{C2}$$

where the coefficient B and the exponent β are real numbers. This approximation ensures that $H(\eta) \to 1$ as $\eta \to 0$, which is a boundary condition requirement in (2.30*a*), when β is a positive real number. Using (C2) in (2.28*b*), we get the first-order approximation for $G(\eta)$ at small values of η as

$$G(\eta) \approx \eta - \frac{B\eta^{\beta+1}}{\beta+1} + C, \tag{C3}$$

where C is a real constant which is independent of η.

We now use (C1), (C2) and (C3) in the boundary layer equations (2.28) to obtain the values of α and β. Using (C1), (C2) in (2.28*c*) and dividing by $-\beta B\eta^{\beta-2}$, we get

$$(\beta - 1) + \tfrac{3}{5}PrA\eta^{\alpha+1} = 0. \tag{C4}$$

Since α is a real number greater than one, the second term on the left-hand side of (C4) goes to zero as $\eta \to 0$. In this limit, $(\beta - 1)$ has to be then zero, i.e.

$$\beta = 1. \tag{C5}$$

Using (C3), (C1) and (C5) in (2.28*a*) and dividing by $\eta^{\alpha-3}$, we obtain

$$5A\alpha(\alpha-1)(\alpha-2) + A^2\alpha(2\alpha-3)\eta^{\alpha+1} - 3B\eta^{5-\alpha} - 2C\eta^{3-\alpha} = 0. \tag{C6}$$

The second term on the left-hand side goes to zero as $\eta \to 0$ since $\alpha > 1$ and is real. In this limit, α has to be then less than 3 for the third and fourth term in (C6) to tend to zero. To balance the equation when $\eta \to 0$, the first term has to be zero. This implies that since $A \neq 0$ and $\alpha > 1$, $\alpha - 2 = 0$, i.e.

$$\alpha = 2. \tag{C7}$$

Using (C5) and (C7), we can re-write (C1), (C2) and (C3) for $\eta \to 0$ as

$$F(\eta) \approx A\eta^2, \quad H(\eta) \approx 1 - B\eta, \quad \text{and} \quad G(\eta) \approx C + \eta - \frac{B}{2}\eta^2. \tag{C8a–c}$$

So we see that for small values of η, $F(\eta)$ is a quadratic function, $H(\eta)$ is a linear function and $G(\eta)$ is a quadratic polynomial in η.

C.2. *For $Pr \gg 1$, the behaviour of $\tilde{F}_1(\tilde{\eta}_1)$, $\tilde{G}_1(\tilde{\eta}_1)$ and $\tilde{H}_1(\tilde{\eta}_1)$ near $\tilde{\eta}_1 = 0$*

A similar first-order approximation as in (C1) and (C2) can be made for $\tilde{F}_1(\tilde{\eta}_1)$ and $\tilde{H}_1(\tilde{\eta}_1)$ in terms of $\tilde{\eta}_1$ as

$$\tilde{F}_1(\tilde{\eta}_1) \approx \tilde{A}\tilde{\eta}_1^{\tilde{\alpha}}, \quad \tilde{H}_1(\tilde{\eta}_1) \approx 1 - \tilde{B}\tilde{\eta}_1^{\tilde{\beta}}, \tag{C9a,b}$$

when $\tilde{\eta}_1 \to 0$. For $\tilde{F}_1'(\tilde{\eta}_1)$ to approach zero and $\tilde{H}_1(\tilde{\eta}_1)$ to approach one when $\tilde{\eta}_1 \to 0$ as per § 4.2*a*, $\tilde{\alpha}$ has to be greater than one and $\tilde{\beta}$ has to be positive. Using (C9) in (4.1*c*) gives

$$(\tilde{\beta} - 1) + \tfrac{3}{5}\tilde{A}\tilde{\eta}_1^{\tilde{\alpha}+1} = 0. \tag{C10}$$

Since $\tilde{\alpha} > 1$, for $\tilde{\eta}_1 \to 0$, the above equation can only be satisfied if

$$\tilde{\beta} = 1. \tag{C11}$$

Using (C9) in (4.1*b*) to find $\tilde{G}$ provides a similar expression as (C3),

$$\tilde{G}_1(\tilde{\eta}_1) \approx \tilde{\eta}_1 - \frac{\tilde{B}\tilde{\eta}^{\tilde{\beta}+1}}{\tilde{\beta}+1} + \tilde{C}, \tag{C12}$$

where $\tilde{C}$ is the constant of integration. Using the above results in (4.1*a*) gives

$$5\tilde{\alpha}(\tilde{\alpha}-1)(\tilde{\alpha}-2)\tilde{A} - \frac{2\tilde{B}\tilde{\beta}}{\tilde{\beta}+1}\tilde{\eta}_1^{5-\tilde{\alpha}} - 2\tilde{C}\tilde{\eta}_1^{3-\tilde{\alpha}} = 0, \tag{C13}$$

where all the terms except the first term goes to zero when $\tilde{\alpha} < 3$ for $\tilde{\eta}_1 \to 0$. Since $\tilde{\alpha} > 1$, (C13) can be satisfied only if

$$\tilde{\alpha} = 2. \tag{C14}$$

So it is found that $\tilde{F}_1$ is quadratic and $\tilde{H}_1$ is linear near $\tilde{\eta}_1$ equals zero.

C.3. *For $Pr \ll 1$, the behaviour of $\tilde{\tilde{F}}_1(\tilde{\tilde{\eta}}_1)$, $\tilde{\tilde{G}}_1(\tilde{\tilde{\eta}}_1)$ and $\tilde{\tilde{H}}_1(\tilde{\tilde{\eta}}_1)$ near $\tilde{\tilde{\eta}}_1 = 0$*

An exactly similar approximation as in (C1) and (C9*a*) is used for $\tilde{\tilde{F}}_1(\tilde{\tilde{\eta}}_1)$ in (4.23*a*) to get

$$5\tilde{\tilde{\alpha}}(\tilde{\tilde{\alpha}}-1)(\tilde{\tilde{\alpha}}-2)\tilde{\tilde{A}} - \tilde{\tilde{A}}^2\tilde{\tilde{\alpha}}(2\tilde{\tilde{\alpha}}-3)\tilde{\tilde{\eta}}_1^{\tilde{\tilde{\alpha}}+1} + \tilde{\tilde{\eta}}_1^{3-\tilde{\tilde{\alpha}}} = 0. \tag{C15}$$

For $\tilde{\tilde{F}}_1'$ to tend to zero, as $\tilde{\tilde{\eta}}_1 \to 0$, $\tilde{\tilde{\alpha}}$ has to be greater than one. So the second and third terms in (C15) tend to zero for $\tilde{\tilde{\alpha}} < 3$ for small $\tilde{\tilde{\eta}}_1$. So (C15) can be satisfied only if

$$\tilde{\tilde{\alpha}} = 2, \tag{C16}$$

implying that $\tilde{\tilde{F}}_1$ is quadratic near $\tilde{\tilde{\eta}}_1$ equals zero.

Appendix D. Rotem & Claassen's (1969) boundary layer parameters

D.1. *Intermediate range of Pr ($O(0.1) \leq Pr \leq O(10)$)*

For $O(0.1) \leq Pr \leq O(10)$, (2.28*a–c*) give the relevant boundary layer equations. The stretched variables used to obtain (2.28) are

$$\hat{y} = y^*_{rc} Gr^{1/5}, \quad \hat{u} = u^*_{rc} Gr^{-2/5} \quad \text{and} \quad \hat{v} = v^*_{rc} Gr^{-1/5}, \tag{D1a–c}$$

where $u^*_{rc} = u/(\nu/L)$ and $v^*_{rc} = v/(\nu/L)$. The similarity transformations used are given by (2.19), (2.20) and (2.21). Velocity components and stream function are related in the usual way as

$$\hat{u} = \frac{\partial \psi^*}{\partial \hat{y}} \quad \text{and} \quad \hat{v} = -\frac{\partial \psi^*}{\partial x^*_{rc}}. \tag{D2a,b}$$

Using (D2*a*), (2.19) and (2.21), we get

$$\hat{u} = {x^*_{rc}}^{1/5} F'(\eta), \tag{D3}$$

while using (D2*b*), (2.19) and (2.21), we get

$$\hat{v} = -\tfrac{3}{5} {x^*_{rc}}^{-2/5} F(\eta) + \tfrac{2}{5} {x^*_{rc}}^{-4/5} \hat{y} F'(\eta). \tag{D4}$$

D.2. *Large Pr ($Pr \gg 1$)*

The stretched variables used to obtain the inner boundary layer equations (4.1) for $Pr \gg 1$ are

$$\tilde{y} = \hat{y} Pr^{1/5}, \quad \tilde{u} = \hat{u} Pr^{3/5} \quad \text{and} \quad \tilde{v} = \hat{v} Pr^{4/5}. \tag{D5a–c}$$

The similarity transformations used are

$$\tilde{\psi} = {x^*_{rc}}^{3/5} \tilde{F}_1(\tilde{\eta}_1), \quad \theta = \tilde{H}_1(\tilde{\eta}_1), \quad \text{and} \quad \tilde{\eta}_1 = \tilde{y} {x^*_{rc}}^{-2/5}. \tag{D6a–c}$$

The pressure function is defined as

$$\tilde{G}_1(\tilde{\eta}_1) = \left(\frac{p - p_\infty}{\rho_\infty \nu^2} L^2 + \frac{g \tilde{y} L^3}{\nu^2} \right) Gr^{-4/5} Pr^{1/5} {x^*_{rc}}^{-2/5}. \tag{D7}$$

From the stream function, we can get the velocity components in the usual way as

$$\tilde{u} = \frac{\partial \tilde{\psi}}{\partial \tilde{y}} \quad \text{and} \quad \tilde{v} = -\frac{\partial \tilde{\psi}}{\partial x^*_{rc}}. \tag{D8a,b}$$

Using (D8), and the definition of stream function and the similarity variable respectively in (D6*a*) and (D6*c*), we can write

$$\tilde{u} = {x^*_{rc}}^{1/5} \tilde{F}'_1(\tilde{\eta}_1) \tag{D9}$$

and

$$\tilde{v} = -\tfrac{3}{5} {x^*_{rc}}^{-2/5} \tilde{F}_1(\tilde{\eta}_1) + \tfrac{2}{5} {x^*_{rc}}^{-4/5} \tilde{y} \tilde{F}'_1(\tilde{\eta}_1). \tag{D10}$$

D.3. *Small Pr (Pr ≪ 1)*

The outer boundary layer equations (4.14) for $Pr \ll 1$ are obtained by using the stretched variables,

$$\tilde{\tilde{x}} = x^*_{rc} Pr^{2/3}, \quad \tilde{\tilde{y}} = \hat{y} Pr^{2/3}, \quad \tilde{\tilde{u}} = \hat{u} Pr^{1/3}, \quad \text{and} \quad \tilde{\tilde{v}} = \hat{v} Pr^{1/3}, \tag{D11a–d}$$

and the similarity transformations,

$$\tilde{\tilde{\psi}} = \tilde{\tilde{x}}^{3/5} \tilde{\tilde{F}}_2(\tilde{\tilde{\eta}}_2), \quad \theta = \tilde{\tilde{H}}_2(\tilde{\tilde{\eta}}_2), \quad \text{and} \quad \tilde{\tilde{\eta}}_2 = \tilde{\tilde{y}} \tilde{\tilde{x}}^{-2/5}. \tag{D12a–c}$$

The pressure function used is

$$\tilde{\tilde{G}}_2(\tilde{\tilde{\eta}}_2) = \left(\frac{p - p_\infty}{\rho_\infty \nu^2} L^2 + \frac{g \tilde{\tilde{y}} L^3}{\nu^2} \right) Gr^{-4/5} Pr^{2/3} \tilde{\tilde{x}}^{-2/5}. \tag{D13}$$

Velocity components are obtained from the stream function as

$$\tilde{\tilde{u}} = \frac{\partial \tilde{\tilde{\psi}}}{\partial \tilde{\tilde{y}}} \quad \text{and} \quad \tilde{\tilde{v}} = -\frac{\partial \tilde{\tilde{\psi}}}{\partial \tilde{\tilde{x}}}. \tag{D14a,b}$$

Using (D12*a*) and (D12*c*) in (D14), we can write

$$\tilde{\tilde{u}} = \tilde{\tilde{x}}^{1/5} \tilde{\tilde{F}}_1'(\tilde{\tilde{\eta}}_1) \tag{D15}$$

and

$$\tilde{\tilde{v}} = \tfrac{3}{5} \tilde{\tilde{x}}^{-2/5} \tilde{\tilde{F}}(\tilde{\tilde{\eta}}) + \tfrac{2}{5} \tilde{\tilde{x}}^{-4/5} \tilde{\tilde{y}} \tilde{\tilde{F}}'(\tilde{\tilde{\eta}}). \tag{D16}$$

D.4. *Conversion of variables from Rotem & Claassen (1969) to Pera & Gebhart (1973)*

A conversion to Pera & Gebhart's (1973) variables is possible from Rotem & Claassen's (1969) and is provided in this section. Dimensional velocity components and temperature are calculated using both Rotem & Claassen's (1969) variables and Pera & Gebhart's (1973) variables, and then equated to obtain the following relationships among them:

$$\eta_{pg} = 5^{-1/5} \eta, \tag{D17}$$

$$\theta(\eta_{pg}) = H(\eta), \quad \theta'(\eta_{pg}) = 5^{1/5} H'(\eta), \tag{D18a,b}$$

$$f(\eta_{pg}) = 5^{-4/5} F(\eta) \quad \text{and} \quad f'(\eta_{pg}) = 5^{-3/5} F'(\eta), \tag{D19a,b}$$

where $\eta_{pg} = (y/x)(Gr_x/5)^{1/5}$ is the similarity variable used by Pera and Gebhart, and $f(\eta_{pg})$ and $\theta(\eta_{pg})$ are the corresponding velocity and temperature functions.

Appendix E. Upper limit of *Ra* for the present analysis

We now estimate the upper limit of the present analysis by estimating the *Ra* at which the local boundary layers would be affected by the external shear due to the global boundary layer, so as to change their nature from a laminar natural convection boundary layer to a mixed convection boundary layer.

Equation (4.10) of Shevkar *et al.* (2023) gives the characteristic velocity (U_c) inside the local boundary layers that are subjected to shear by the global boundary layers. These are given as a perturbation series in Péclet number (Pe_λ) based on U_c and the no-shear plume spacing λ_0 as

$$Pe_\lambda = Pe_{\lambda 0} + \epsilon Pe_{\lambda 1} + \epsilon Pe_{\lambda 2} + O(\epsilon^3), \tag{E1}$$

where

$$\epsilon = Re_\lambda / Ra_\lambda \tag{E2}$$

is a small parameter with $Re_\lambda = V_F \lambda_0 / \nu$ and $Ra_\lambda = g\beta \Delta T_w \lambda_0^3 / \nu\alpha$ being the Reynolds and Rayleigh numbers based on λ_0, with V_F being the large-scale flow velocity and ΔT_w the temperature drop across the local boundary layer. There is no effect of shear on the local boundary layers when

$$\epsilon Pe_{\lambda 1} < Pe_{\lambda 0} \tag{E3}$$

in (E1).

As given by Shevkar *et al.* (2023),

$$Pe_{\lambda 0} = \left(\frac{C_2}{8E}\right)^{2/5} Ra_\lambda^{2/5} \tag{E4}$$

and

$$Pe_{\lambda 1} = \frac{A Ra_\lambda}{5EPr^n}, \tag{E5}$$

where $E = f(Pr) = 5$ for $Pr = 0.7$, $n = 0.5$, $C_2 = 0.72$, $A = u|_{z=\delta}/V_F$, the dimensionless velocity at the edge of the local boundary layer. The Re_λ in (E2) can be rewritten as

$$Re_\lambda = Re(\lambda / Z_w)(Z_w / H), \tag{E6}$$

with

$$\lambda / Z_w = Ra_\lambda^{1/3} = C_1 Pr^{n_1}, \tag{E7}$$

$$Z_w / H = (2/Ra)^{1/3} \tag{E8}$$

and

$$Re = V_F H / \nu = 1.169 Ra^{4/9} Pr^{-2/3} \Gamma^{-0.57}, \tag{E9}$$

where Γ is the aspect ratio of the convection cell (Shevkar *et al.* 2023), $C_1 = 47.5$, $n_1 = 0.1$ and $Z_w = (\nu\alpha / g\beta\Delta T_w)^{1/3}$ the near-wall length scale in convection (Puthenveettil *et al.* 2011). Substituting (E7), (E8) and (E9) in (E6), and the resulting Re_λ in (E2), with Ra_λ from (E7), we obtain

$$\epsilon = \frac{2^{1/3} 1.169}{C_1^2 Pr^{2/3+2n_1} \Gamma^{0.57}} Ra^{1/9}. \tag{E10}$$

Substituting (E4), (E5) and (E10) in (E3), we obtain the Rayleigh number below which shear does not affect the local boundary layers as

$$Ra^{1/9} < \left(\frac{C_1 C_2^2 E^3}{8}\right)^{1/5} \frac{5}{2^{1/3} 1.169} \frac{\Gamma^{0.57}}{A} Pr^{n_1/5+n+2/3}. \tag{E11}$$

Since the thickness of the local boundary layers are an order smaller than the thickness of the global boundary layer, $A \simeq 0.1$. Then for $Pr = 0.7$, at $\Gamma = 1$, the local boundary

layers are not affected by the shear due to the global boundary layer at

$$Ra < 1.45 \times 10^{15}. \tag{E12}$$

Since the present study is limited to the case were the local boundary layers retain their natural convection boundary layer nature, (E12) gives the upper limit of the present study.

Appendix F. Validity of Oberbeck–Boussinesq (OB) approximation in the present study

The violation of OB approximation due to temperature variations occurs (Barletta 2022) when

$$\beta \Delta T > 1. \tag{F1}$$

The smaller the value of $\beta \Delta T$, the better the approximation. For the case of air that we consider in the present study, since $\beta \simeq 1/T_{ref}$, (F1) gives a value of

$$\Delta T > T_{ref} \tag{F2}$$

for the violation of OB approximation. For the usually encountered bulk temperature of $T_{ref} \simeq 25\,^{\circ}\mathrm{C}$, (F2) then means that $\Delta T > 25\,^{\circ}\mathrm{C}$, for the violation of the OB approximation. This is of similar order to the value of $\Delta T > 28.6\,^{\circ}\mathrm{C}$ obtained by Gray & Giorgini (1976) for air at $15\,^{\circ}\mathrm{C}$ using a more rigorous analysis. The present study is limited to the case where the temperature difference across the boundary layer thickness is $\Delta T_w < 10\,^{\circ}\mathrm{C}$. Hence, the OB approximation is far from violated in the present study.

Alternatively, the OB approximation also gets violated when the length scales involved become large, so that the Gebhart number

$$Ge = g\beta L/C_p > 1 \tag{F3}$$

for small fixed temperature differences (Barletta 2022). For a bulk temperature of $25\,^{\circ}\mathrm{C}$ for air, (F3) gives $L > 3.06 \times 10^4$ m for the OB approximation to be violated. The length scales of boundary layers in the present case are of the order of mm. Hence, the OB approximation is far from violated in the present study under this consideration too.

Appendix G. Validity of the present study to turbulent RBC

The present study finds the scaling of dust-free region heights in laminar natural convection boundary layers over horizontal surfaces, and proposes that the same scaling of dust-free region heights could be expected in turbulent RBC. However, there are strong fluctuations near the plate in turbulent RBC, of the order of the mean quantities themselves, which makes the validity of the present analysis to turbulent RBC somewhat unclear. We now clarify this apparent contradiction below.

In turbulent RBC, it is well known that a shear boundary layer is created by the large-scale flow, which we call as the global boundary layer since it spans the length of the convection cell. This global boundary layer has been the concern of most of the scaling theories of RBC so far, with many assumptions about their nature, ranging from laminar zero pressure gradient shear boundary layer (Grossman & Lohse 2000) to turbulent shear boundary layer (Siggia 1994). However, the dominant coherent structures on the hot and cold plate in RBC are line plumes. These plumes are the long-time outcomes of instability of boundary layers at their bases. It then follows that, in addition to the global boundary layer, there have to be boundary layers in between these plumes, which we refer to as local boundary layers. Figure 11 shows the global and the local boundary layers.

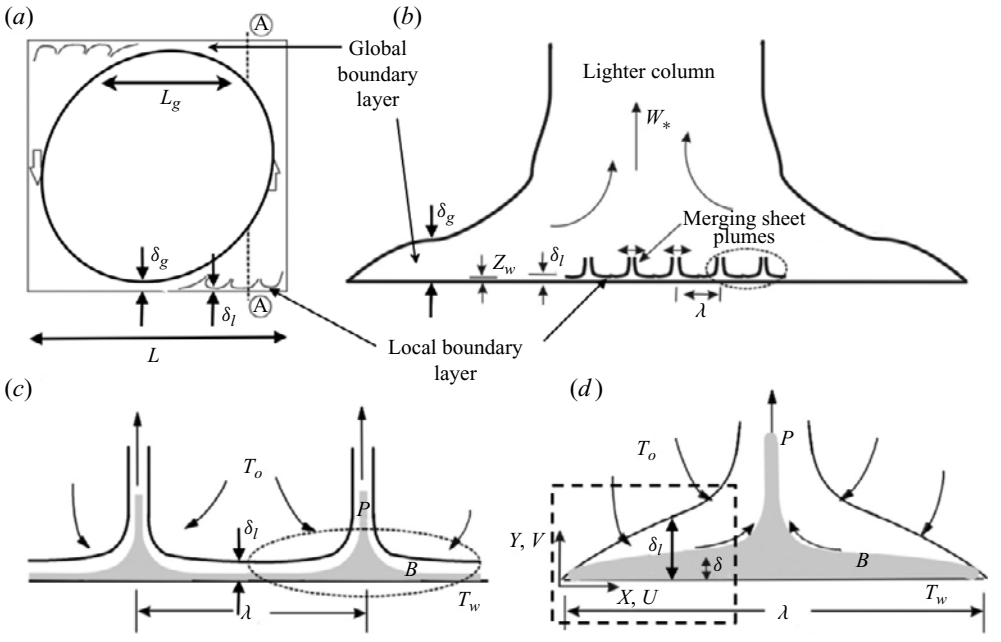

Figure 11. (*a*) Schematic of the large-scale flow, the global boundary layer and the plumes on the plates along with the local boundary layers in between them. (*b*) Side view of the vertical section in A–A in a plane perpendicular to the plane in panel (*a*), showing the local plumes driving the large scale flow (Puthenveettil *et al.* 2011). (*c*) Zoomed view of the local boundary layers and plumes in the region shown with the dashed ellipse in panel (*b*). *B* denotes local boundary layer and *P* the plume. The lines show the edges of the local velocity boundary layer and the velocity boundary layer of the plume, while the shaded regions show the local thermal boundary layer and the thermal boundary layer of the plume. (*d*) Zoomed view of the dashed ellipse in panel (*c*) showing the details of one plume and two local boundary layers at its base (Theerthan & Arakeri 1998).

As shown by Shevkar *et al.* (2023), the ratio of the thickness of the local to the global boundary layer $\delta_l/\delta_g \sim Ra^{-1/9}$; then for the range of the present study, $1 \times 10^6 \leq Ra \leq 1 \times 10^{15}$, $0.2 \leq \delta_l/\delta_g \leq 0.02$. The length of the local boundary layers are decided by their instability, which decide when they turn upwards to form plumes. As given by Puthenveettil *et al.* (2011), the length of the local boundary layers,

$$\lambda = C_1 Pr^{n_1} Z_w, \tag{G1}$$

where Z_w (2.3) is the near-plate length scale in turbulent convection, $C_1 = 47.5$ and $n_1 = 0.1$. As shown in figure 11, the length of the global boundary layer $L_g \sim L$. Then, for aspect ratio $\Gamma = 1$,

$$\frac{\lambda}{L_g} = \frac{2^{1/3} C_1 Pr^{n_1}}{Ra^{1/3}} \tag{G2}$$

for $1 \times 10^6 \leq Ra \leq 1 \times 10^{15}$, $0.58 \leq \lambda/L_g \leq 5.8 \times 10^{-4}$. The local boundary layers are then an order smaller in thickness ($\delta_l \ll \delta_g$) and length ($\lambda \ll L_g$) than the global boundary layers and are hence embedded within the global boundary layers.

The global boundary layers are most likely turbulent, even at moderate *Ra*, since the bulk flows that cause them are turbulent in turbulent RBC. In contrast, the thin local boundary layers, which are embedded within these global boundary layers, are most likely laminar.

This is so since plumes are outcomes of the spatial instability of these local boundary layers at their bases, then, the local boundary layers themselves, since they exist before their spatial instability has developed, have to be laminar. This hypothesis – of two local laminar natural convection boundary layers, giving rise to plumes, being the dominant coherent structure on the plates in turbulent RBC – has since been proved in the following multiple studies. The predictions based on the above hypothesis of (i) the mean plume spacings (Theerthan & Arakeri 1998; Puthenveettil 2004; Puthenveettil & Arakeri 2005), (ii) the total length of plumes (Puthenveettil *et al.* 2011), (iii) the mean merging velocity of plumes (Gunasegarane & Puthenveettil 2014), (iv) the mean time for the appearance of plumes at a vacant spot (Gunasegarane & Puthenveettil 2014), (v) the mean plume spacing in the presence of shear (Shevkar *et al.* 2019) and (vi) the scaling of the peaks of the horizontal velocity distributions (Shevkar *et al.* 2023), all done at large *Ra* too, have been shown to match with measurements from experimental and computational studies of turbulent RBC.

It is also known that there is no contradiction in the presence of fluctuations near the plate and within the global boundary layers, with the above assumption of laminar nature of local boundary layers. This is so since these fluctuations close to the plate are partly caused by the motion of these laminar local boundary layers and the plumes themselves, so that a local measurement at a fixed point would measure properties from local boundary layers, plumes and the turbulent bulk at different times, each of these having different values, the time series then appearing as a fluctuating signal. This phenomenology has substantial proof since the vertical profiles of vertical velocity fluctuations, temperature fluctuations and mean temperature in turbulent RBC have all been predicted well by Theerthan & Arakeri (1998) using a model that assumes that the flow near the plate is made up of a uniform array of pairs of local laminar boundary layers, each pair giving rise to a laminar line plume, so that the plumes are equally spaced, equal to the mean plume spacing observed in experiments.

The majority of the temperature drop near the plate occurs across these local boundary layers, and hence, the formation of the dust-free region, driven by the temperature difference induced thermophoresis, will occur within the local boundary layers, which, as we saw earlier, is anyway within the global boundary layer. The local boundary layer and not the global boundary layer is hence the relevant flow and temperature field that needs to be studied to analyse the formation of a dust-free region near horizontal hot surfaces in turbulent RBC. The flow field used in the present study could then be considered to be that within the local boundary layers in turbulent RBC, which could be very well assumed to be laminar natural convection boundary layers due to the reasons mentioned above. In the present study, as seen in figure 6, the dimensionless height of the dust-free regions (η_{df}), except for large values of Th_m ($Th_m > 10^4$) and low values of Prandtl number ($Pr < 0.3$), is around 10 for $Pr = 0.3$ and around 5 for $Pr = 10$ at $Th_m = 10^4$; the heights being less at lower Th_m. The corresponding dimensionless heights of natural convection boundary layers for $0.1 < Pr < 10$, as given by Rotem & Claassen (1969) are $15 < \eta < 6$. As expected, then $\eta_{df}/\eta < 1$ for $Th_m < 10^4$ and $Pr > 0.3$, the dust-free region heights are much smaller than the corresponding local boundary layer thicknesses. The above assumption of laminar natural convection nature of the local boundary layers turbulent RBC is likely to be violated at large *Ra* where the shear due to the global boundary layer changes the nature of these local boundary layers to that of a mixed convection boundary layer; the limit for such a change is given in Appendix E.

References

AITKEN, J. 1884 On the formation of small clear spaces in dusty air. *Earth Environ. Sci. Trans. R. Soc. Edin.* **32** (2), 239–272.

BARLETTA, A. 2022 The Boussinesq approximation for buoyant flows. *Mech. Res. Commun.* **124**, 103939.

BATCHELOR, G.K. & SHEN, C. 1985 Thermophoretic deposition of particles in gas flowing over cold surfaces. *J. Colloid Interface Sci.* **107** (1), 21–37.

BERESNEV, S. & CHERNYAK, V. 1995 Thermophoresis of a spherical particle in a rarefied gas: numerical analysis based on the model kinetic equations. *Phys. Fluids* **7** (7), 1743–1756.

BERGOUGNOUX, L., BOUCHET, G., LOPEZ, D. & GUAZZELLI, E. 2014 The motion of solid spherical particles falling in a cellular flow field at low Stokes number. *Phys. Fluids* **26** (9), 093302.

BESLING, W.F.A., VAN DER PUT, P.J.J.M. & SCHOONMAN, J. 1995 Laser-induced chemical vapour deposition of silicon carbonitride. *J. Phys. IV* **5** (C5), C5–953–960.

CANDELIER, F., MEHLIG, B. & MAGNAUDET, J. 2019 Time-dependent lift and drag on a rigid body in a viscous steady linear flow. *J. Fluid Mech.* **864**, 554–595.

CAWOOD, W. 1936 The movement of dust or smoke particles in a temperature gradient. *Trans. Faraday Soc.* **32**, 1068–1073.

EISNER, A.D. & ROSNER, D.E. 1985 Experimental studies of soot particle thermophoresis in nonisothermal combustion gases using thermocouple response techniques. *Combust. Flame* **61** (2), 153–166.

EPSTEIN, M., HAUSER, G.M. & HENRY, R.E. 1985 Thermophoretic deposition of particles in natural convection flow from a vertical plate. *J. Heat Transfer* **107** (2), 272–276.

FERNANDES, A. & LOYALKA, S.K. 1996 Modeling of thermophoretic deposition of aerosols in nuclear reactor containments. *Nucl. Technol.* **116** (3), 270–282.

GOKOGLU, S.A. & ROSNER, D.E. 1986 Thermophoretically augmented mass transfer rates to solid walls across laminar boundary layers. *AIAA J.* **24** (1), 172–179.

GOREN, S.L. 1977 Thermophoresis of aerosol particles in the laminar boundary layer on a flat plate. *J. Colloid Interface Sci.* **61** (1), 77–85.

GRAY, D.D. & GIORGINI, A. 1976 The validity of the boussinesq approximation for liquids and gases. *Intl J. Heat Mass Transfer* **19** (5), 545–551.

GROSSMAN, S. & LOHSE, D. 2000 Scaling in thermal convection: a unifying theory. *J. Fluid Mech.* **407**, 27–56.

GUHA, A. 2008 Transport and deposition of particles in turbulent and laminar flow. *Annu. Rev. Fluid Mech.* **40**, 311–341.

GUHA, A. & SAMANTA, S. 2014 Effect of thermophoresis and its mathematical models on the transport and deposition of aerosol particles in natural convective flow on vertical and horizontal plates. *J. Aerosol Sci.* **77**, 85–101.

GUNASEGARANE, G.S. & PUTHENVEETTIL, B.A. 2014 Dynamics of line plumes on horizontal surfaces in turbulent convection. *J. Fluid Mech.* **749**, 37–78.

GUPTA, V., SHARMA, M., PACHAURI, R.K. & BABU, K.N.D. 2019 Comprehensive review on effect of dust on solar photovoltaic system and mitigation techniques. *Solar Energy* **191**, 596–622.

HOMSY, G.M., GEYLING, F.T. & WALKER, K.L. 1981 Blasius series for thermophoretic deposition of small particles. *J. Colloid Interface Sci.* **83** (2), 495–501.

MARTIN, D. & NOKES, R. 1988 Crystal settling in a vigorously converting magma chamber. *Nature* **332** (6164), 534–536.

MAXEY, M.R. & CORRSIN, S. 1986 Gravitational settling of aerosol particles in randomly oriented cellular flow fields. *J. Atmos. Sci.* **43** (11), 1112–1134.

MAXEY, M.R. & RILEY, J.J. 1983 Equation of motion for a small rigid sphere in a nonuniform flow. *Phys. Fluids* **26** (4), 883–889.

NAZAROFF, W.W. & CASS, G.R. 1987 Particle deposition from a natural convection flow onto a vertical isothermal flat plate. *J. Aerosol Sci.* **18** (4), 445–455.

NICHOLSON, K.W. 1988 A review of particle resuspension. *Atmos. Environ. (1967)* **22** (12), 2639–2651.

OH, S., FIGGIS, B.W. & RASHKEEV, S. 2020 Effects of thermophoresis on dust accumulation on solar panels. *Solar Energy* **211**, 412–417.

PATRA, P., KOCH, D.L. & ROY, A. 2022 Collision efficiency of non-Brownian spheres in a simple shear flow – the role of non-continuum hydrodynamic interactions. *J. Fluid Mech.* **950**, A18.

PERA, L. & GEBHART, B. 1973 Natural convection boundary layer flow over horizontal and slightly inclined surfaces. *Intl J. Heat Mass Transfer* **16** (6), 1131–1146.

PUTHENVEETTIL, B.A. 2004 Investigations on high Rayleigh number turbulent free-convection. PhD thesis, Indian Institute of Science, Bangalore, India.

PUTHENVEETTIL, B.A. & ARAKERI, J.H. 2005 Plume structure in high Rayleigh number convection. *J. Fluid Mech.* **542**, 217–249.

PUTHENVEETTIL, B.A., GUNASEGARANE, G.S., AGRAWAL, Y.K., SCHMELING, D., BOSBACH, J. & ARAKERI, J.H. 2011 Length of near-wall plumes in turbulent convection. *J. Fluid Mech.* **685**, 335–364.

PUTRA, N., ROETZEL, W. & DAS, S.K. 2003 Natural convection of nano-fluids. *Heat Mass Transfer* **39** (8–9), 775–784.

ROTEM, Z. & CLAASSEN, L. 1969 Free convection boundary-layer flow over horizontal plates and discs. *Can. J. Chem. Engng* **47** (5), 461–468.

SAFFMAN, P.G. 1965 The lift on a small sphere in a slow shear flow. *J. Fluid Mech.* **22** (2), 385–400.

SAMANTA, S. & GUHA, A. 2012 A similarity theory for natural convection from a horizontal plate for prescribed heat flux or wall temperature. *Intl J. Heat Mass Transfer* **55** (13–14), 3857–3868.

SAPSIS, T. & HALLER, G. 2008 Instabilities in the dynamics of neutrally buoyant particles. *Phys. Fluids* **20** (1), 017102.

SHEVKAR, P.P., GUNASEGARANE, G.S., MOHANAN, S.K. & PUTHENVEETTIL, B.A. 2019 Effect of shear on coherent structures in turbulent convection. *Phys. Rev. Fluids* **4** (4), 043502.

SHEVKAR, P.P., MOHANAN, S.K. & PUTHENVEETTIL, B.A. 2023 Effect of shear on local boundary layers in turbulent convection. *J. Fluid Mech.* **962**, A41.

SHEVKAR, P.P., VISHNU, R., MOHANAN, S.K., KOOTHUR, V., MATHUR, M. & PUTHENVEETTIL, B.A. 2022 On separating plumes from boundary layers in turbulent convection. *J. Fluid Mech.* **941**, A5.

SIGGIA, E.D. 1994 High Rayleigh number convection. *Annu. Rev. Fluid Mech.* **26** (1), 137–168.

STRATMANN, F., FISSAN, H., PAPPERGER, A. & FRIEDLANDER, S. 1988 Suppression of particle deposition to surfaces by the thermophoretic force. *Aerosol Sci. Technol.* **9** (2), 115–121.

TALBOT, L., CHENG, R.K., SCHEFER, R.W. & WILLIS, D.R. 1980 Thermophoresis of particles in a heated boundary layer. *J. Fluid Mech.* **101** (4), 737–758.

THEERTHAN, S.A. & ARAKERI, J.H. 1998 A model for near-wall dynamics in turbulent Rayleigh–Bénard convection. *J. Fluid Mech.* **373**, 221–254.

TYNDALL, J. 1870 On dust and disease. *Fraser's Mag.* **1** (3), 302–310.

WEN, J. & WEXLER, A.S. 2007 Thermophoretic sampler and its application in ultrafine particle collection. *Aerosol Sci. Technol.* **41** (6), 624–629.

YANG, W., ZHANG, Y., WANG, B., DONG, Y. & ZHOU, Q. 2022 Dynamic coupling between carrier and dispersed phases in Rayleigh–Bénard convection laden with inertial isothermal particles. *J. Fluid Mech.* **930**, A24.

ZERNIK, W. 1957 The dust-free space surrounding hot bodies. *Br. J. Appl. Phys.* **8** (3), 117–120.